Atmos. Chem. Phys., 21, 13077–13098, 2021
https://doi.org/10.5194/acp-21-13077-2021

Atmospheric Chemistry and Physics
Open Access
EGU

Isotopic evidence for dominant secondary production of HONO in near-ground wildfire plumes

Jiajue Chai[1,2], Jack E. Dibb[3], Bruce E. Anderson[4], Claire Bekker[1,2], Danielle E. Blum[1,5], Eric Heim[3], Carolyn E. Jordan[4,6], Emily E. Joyce[1,2], Jackson H. Kaspari[7], Hannah Munro[3], Wendell W. Walters[1,2], and Meredith G. Hastings[1,2]

[1]Institute at Brown for Environment and Society, Brown University, Providence, RI, USA
[2]Department of Earth, Environmental and Planetary Sciences, Brown University, Providence, RI, USA
[3]Institute for the Study of Earth, Oceans and Space, University of New Hampshire, Durham, NH, USA
[4]NASA Langley Research Center, Hampton, VA, USA
[5]Department of Chemistry, Brown University, Providence, RI, USA
[6]National Institute of Aerospace, Hampton, VA, USA
[7]Department of Chemistry, University of New Hampshire, Durham, NH, USA

Correspondence: Jiajue Chai (jiajue_chai@brown.edu)

Received: 13 March 2021 – Discussion started: 29 March 2021
Revised: 21 July 2021 – Accepted: 3 August 2021 – Published: 3 September 2021

Abstract. Nitrous acid (HONO) is an important precursor to hydroxyl radical (OH) that determines atmospheric oxidative capacity and thus impacts climate and air quality. Wildfire is not only a major direct source of HONO, it also results in highly polluted conditions that favor the heterogeneous formation of HONO from nitrogen oxides ($NO_x = NO + NO_2$) and nitrate on both ground and particle surfaces. However, these processes remain poorly constrained. To quantitatively constrain the HONO budget under various fire and/or smoke conditions, we combine a unique dataset of field concentrations and isotopic ratios ($^{15}N / ^{14}N$ and $^{18}O / ^{16}O$) of NO_x and HONO with an isotopic box model. Here we report the first isotopic evidence of secondary HONO production in near-ground wildfire plumes (over a sample integration time of hours) and the subsequent quantification of the relative importance of each pathway to total HONO production. Most importantly, our results reveal that nitrate photolysis plays a minor role (<5 %) in HONO formation in daytime aged smoke, while NO_2-to-HONO heterogeneous conversion contributes 85 %–95 % to total HONO production, followed by OH + NO (5 %–15 %). At nighttime, heterogeneous reduction of NO_2 catalyzed by redox active species (e.g., iron oxide and/or quinone) is essential (≥ 75 %) for HONO production in addition to surface NO_2 hydrolysis. Additionally, the $^{18}O / ^{16}O$ of HONO is used for the first time to constrain the NO-to-NO_2 oxidation branching ratio between ozone and peroxy radicals. Our approach provides a new and critical way to mechanistically constrain atmospheric chemistry and/or air quality models on a diurnal timescale.

1 Introduction

Vastly increased wildfire activity and intensity is a challenging issue in many parts of the world including the western US, and it is strongly linked to warming surface temperatures and earlier spring snowmelt (Westerling, 2016). Wildfire is a significant source of nitrogen oxides ($NO_x = NO + NO_2$) and nitrous acid (HONO), as well as other important trace gases and particulate matter. NO_x serves as a key precursor to atmospheric ozone (O_3) and secondary aerosols in the presence of organic compounds; in wildfire plumes NO_x can be a limiting factor to O_3 production owing to high emission molar ratios of non-methane organic carbon (NMOC) to NO_x (Akagi et al., 2011; Jaffe and Briggs, 2012). HONO is a major daytime photolytic precursor of hydroxyl radical (OH) via Reaction (R1) that determines the atmospheric oxidative capacity and therefore the lifetimes of many other species in the atmosphere. Wildfire-emitted HONO supplies the majority of OH in the first few hours after smoke emission in the day-

time, and it greatly counteracts reduced OH production from O_3 photolysis caused by high particle loading reducing actinic flux (Jaffe and Briggs, 2012; Peng et al., 2020; Theys et al., 2020). Wildfire-emitted NO_x and HONO not only greatly impact the atmospheric chemistry in local regions close to the fire but also contribute significantly to the reactive nitrogen (RN) burden thousands of kilometers downwind via transport and RN cycling, especially when mixed with fossil fuel combustion emissions (Jaffe et al., 2013; McClure and Jaffe, 2018; Westerling et al., 2006; Westerling, 2016).

$$\mathrm{HONO}(g) \xrightarrow{h\nu} \mathrm{OH} + \mathrm{NO} \quad \text{(R1)}$$

Despite their important impacts on air quality, climate, and human and ecosystem health, the budgets of wildfire-derived NO_x and HONO are poorly constrained due to limited field measurements, high reactivity and large spatiotemporal heterogeneity. Bottom-up approaches rely on limited emission factor measurements with uncertainty in HONO sources and chemistry; top-down approaches (i.e., satellite observations) have limited sensitivity in the lower troposphere and boundary layer and again are limited by large uncertainties in HONO sources and chemistry to interpret the satellite measurements. Although gas-phase reaction between OH and NO (Reaction R2) ubiquitously produces HONO, it is far from sufficient to explain the observed HONO levels in numerous studies given the fast photolysis during the day (Su et al., 2011). HONO, along with NO_x, can be directly emitted from various sources including vehicle exhaust, biomass burning (BB) and microbially driven soil emissions. In addition, it has been proposed that HONO can be produced from other RN species (e.g., NO_2 and nitrate) via various heterogeneous pathways (Fig. 1). Major secondary HONO production pathways during the day include heterogeneous NO_2 conversion on photoactive surfaces (Reaction R3) (Ammann et al., 1998; George et al., 2005; Stemmler et al., 2006) and heterogeneous photolysis of nitrate including particulate nitrate ($p\text{-}NO_3^-$) and nitric acid (HNO_3) via Reaction (R4) (Ye et al., 2016; Zhou et al., 2011). In past studies, heterogeneous conversion of NO_2 to HONO on photoactive surfaces such as organic surfaces (Reaction R3) has been proposed to explain a missing HONO source (Ammann et al., 1998; George et al., 2005; Stemmler et al., 2006; Wong et al., 2012). Organic surfaces exist in both aerosol particles and soils at the surface (e.g., humic acids), but there is major uncertainty associated with quantifying available surface area and the NO_2 uptake coefficient. During the night, surface (soils and aerosols) uptake is the predominant sink for HONO (Reaction R5), and heterogeneous conversion of NO_2 to HONO has been widely accepted as the major secondary HONO production source during the night (Reaction R6 and/or Reaction R7). Although it is clear that heterogeneous NO_2 hydrolysis (Reaction R6) can be a major pathway for nighttime HONO production (Finlayson-Pitts et al., 2003), recent work has also shown compelling evidence for faster HONO formation via reduction of NO_2 on inorganic surfaces (e.g., iron-bearing minerals) and organic surfaces (e.g., quinone-rich humic acid) in soils and particulate matter (Reaction R7) (Scharko et al., 2017; Kebede et al., 2016; Martins-Costa et al., 2020). While the emission sources and heterogeneous pathways were hypothetically used to account for missing HONO sources (Stemmler et al., 2006; Su et al., 2011; Ye et al., 2016; VandenBoer et al., 2014; Donaldson et al., 2014a; Kebede et al., 2016; Scharko et al., 2017), their relative importance is poorly quantified due to large uncertainties associated with emission heterogeneity, surface area and composition, environmental condition (day versus night, temperature, relative humidity), quantification of heterogeneous reaction rate, and knowledge gaps in detailed mechanisms. As a result, the HONO budget in the atmospheric boundary layer remains poorly constrained.

$$\mathrm{HO} + \mathrm{NO} + M \rightarrow \mathrm{HONO} + M \quad (M = \text{third body gas molecules, e.g., nitrogen}) \quad \text{(R2)}$$

$$\mathrm{NO_2}(g) + \mathrm{DSS} \xrightarrow{h\nu} \mathrm{HONO} + \mathrm{DSS} \quad (g = \text{gas; DSS} = \text{daytime surface substrate}) \quad \text{(R3)}$$

$$\mathrm{HNO_3} \xrightarrow{h\nu} \mathrm{HONO} + \mathrm{O} \quad \text{(R4)}$$

$$\mathrm{HONO}(g) \rightarrow \mathrm{HONO}(a) \quad (a = \text{adsorbed to surfaces}) \quad \text{(R5)}$$

$$2\mathrm{NO_2}(a) + \mathrm{H_2O}(a) \rightarrow \mathrm{HONO} + \mathrm{HNO_3} \quad \text{(R6)}$$

$$\mathrm{NO_2}(a) + \mathrm{NSS} \rightarrow \mathrm{HONO} + \mathrm{NSS} \quad (\mathrm{NSS} = \text{nighttime surface substrate}) \quad \text{(R7)}$$

Stable isotopes hold unique promise to provide rigorous constraints on sources, chemical processing pathways and sinks of RN species as they reflect isotopic signatures associated with these processes. $\delta^{15}N$ $(= [(^{15}N / {}^{14}N)_{sample} / (^{15}N / {}^{14}N)_{air-N_2} - 1] \times 1000‰)$ has shown great potential to trace the atmospheric origin of NO_x and its fate as nitrate (Hastings et al., 2009), whereas $\delta^{18}O$ $(= [(^{18}O / {}^{16}O)_{sample} / (^{18}O / {}^{16}O)_{VSMOW} - 1] \times 1000‰$; VSMOW is Vienna Standard Mean Ocean Water) serves as a sensitive indicator for the relative importance of major oxidants (i.e., O_3, RO_2 and OH) that lead to NO_x conversion (Thiemens, 2006). In particular, O_3 has an exclusively high $\delta^{18}O$ as a result of mass-independent fractionation associated with its formation in the atmosphere, and this anomaly is transferred to oxidized products such as NO_2, HONO and HNO_3 (Thiemens, 2006).

Using our recently developed and validated sampling techniques in combination with offline isotopic composition analyses (Chai et al., 2019), we characterized for the first time $\delta^{15}N$ of NO_x and HONO, as well as $\delta^{18}O$-HONO, in ground-level wildfire plumes in the western US as part of two major field campaigns: Western Wildfire Experiment for Cloud Chemistry, Aerosol Absorption and Nitrogen (WECAN) in summer 2018 and Fire Influence on Regional and

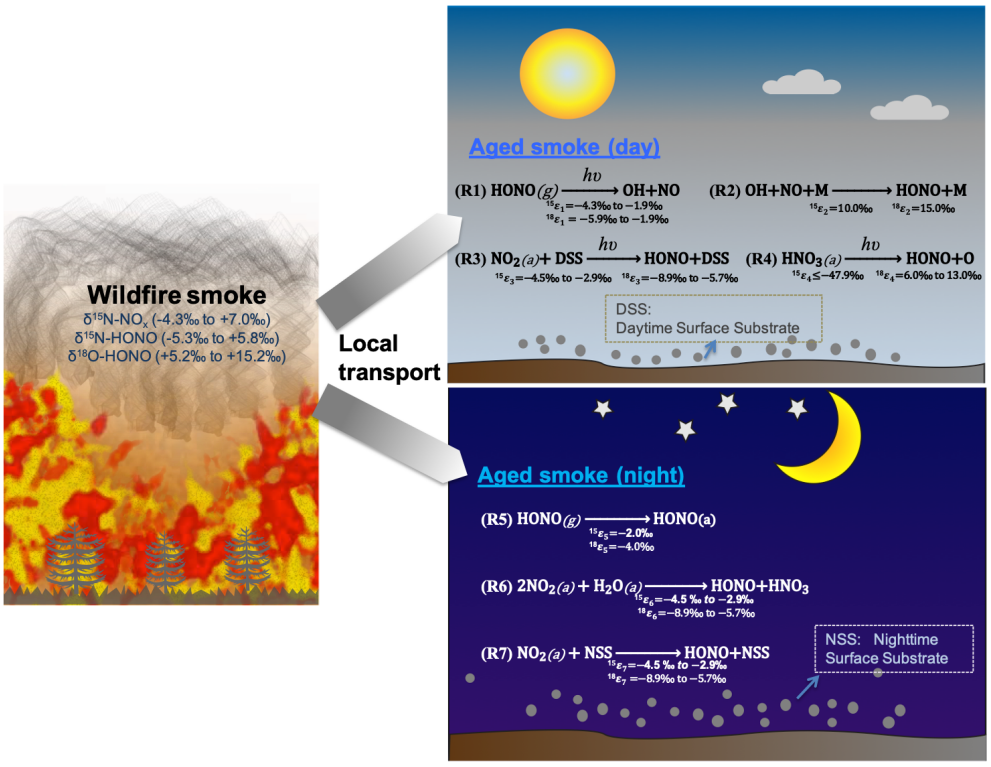

Figure 1. The schematics of loss and secondary production of HONO in areas impacted by wildfire smoke in daytime (Reactions R1–R4) and nighttime (Reactions R5–R7). We conducted our sample collection <30 km from the edge of the wildfires, with smoke ages ranging from a few minutes to half a day. M is bath gas including N_2, O_2, CO_2, etc. DSS is daytime substrate surface including terrestrial surfaces and aerosol particles that incorporate photoactive metal oxides (e.g., TiO_2), humic-like organics (e.g., quinone), etc. In essence, solar radiation induces reduction of these substrates with H, and this facilitates H abstraction by NO_2 (or H transfer). NSS is nighttime substrate surface (terrestrial and aerosol surfaces) containing iron-bearing minerals and/or humic acid (quinone). Note other sinks during both day and night (e.g., OH + HONO) are negligible compared to the major sinks shown here. Isotopic enrichment factors for N and O result from kinetic isotopic effects associated with each reaction and are calculated and expressed as $^{15}\varepsilon_i$ and $^{18}\varepsilon_i$, where the subscript i indicates the reaction number, and the superscripts 15 and 18 denote the isotopic composition $^{15}N/^{14}N$ and $^{18}O/^{16}O$, respectively.

Global Environments Experiment – Air Quality (FIREX-AQ) in summer 2019. Here we report our findings based on samples collected in a mobile laboratory platform from three different wildfires; Rabbit Foot fire (RF) in eastern Idaho, Williams Flats fire (WF) in central Washington, and Nethker fire (NF) in northern Idaho (Figs. S1 and S2 in the Supplement). Surface-based mobile sampling allowed us to characterize young nighttime (YN), young daytime (YD), mixed daytime (MD), aged nighttime (AN) and aged daytime (AD) smoke. Physical smoke age determination using meteorological parameters near the ground is challenging due to large variations in wind speed and direction. Proxies involving total RN, NO_y and ammonia (NH_3) relative to carbon monoxide (CO) can only be used to qualitatively evaluate smoke age due to large uncertainties in source emission factors and complexity caused by photochemistry (Selimovic et al., 2019; Kleinman et al., 2007). In contrast, the concentration ratio between $PM_{2.5}$ and CO ($PM_{2.5}$ / CO) has shown potential for estimating smoke age (Yokelson et al., 2009; Selimovic et al., 2020). In this work, we determined the smoke conditions (young versus aged) primarily by comparing the field δ^{18}O-HONO results with those obtained in our previous lab study that represents fresh emissions, with additional evaluation involving δ^{15}N-HONO and relative concentration of HONO and NO_2 (Fig. 2). Note young and aged smoke refers to negligible and large proportions of secondarily produced HONO, respectively. We also take into account smoke sampling locations (i.e., approximate distance from the wildfire) to confirm the smoke age estimate. In brief, largely elevated δ^{18}O-HONO in field samples compared with those from the lab-controlled fires signifies significant atmospheric processing, and this will be discussed in detail below. Our grouping method using δ^{18}O-HONO shows fairly consistent results with those suggested by $PM_{2.5}$ / CO for WF and NF fire plumes (Kaspari et al., 2021). In addition to distinguishing aged smoke from young smoke, the grouped δ^{18}O and δ^{15}N also allow us to characterize potential mechanisms of secondary HONO formation in the aged smoke, as well as NO-to-NO_2 oxidation pathways, with the HONO budget evalu-

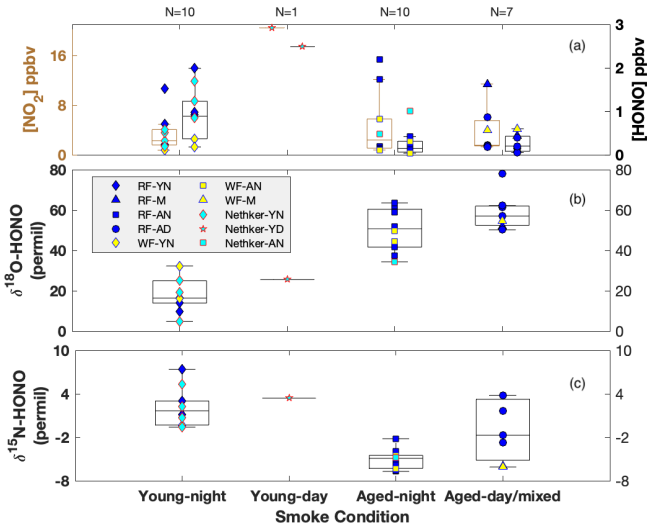

Figure 2. Box-whisker plots for concentration of NO_2 (left) and HONO (right) **(a)**, δ^{18}O-HONO **(b)** and δ^{15}N-HONO **(c)** for each sample. Individual data points are plotted within each box grouped by various field smoke conditions including young nighttime smoke (YN), young daytime smoke (YD), mixed daytime smoke (M) that contains smoke contributed by either night smoke or fresh smoke, aged nighttime smoke (AN) and aged daytime smoke (AD). Data from three wildfires are shown here, including Rabbit Foot (RF) fire during the 2018 WE-CAN campaign, Williams Flats (WF) fire and Nethker fire during the 2019 FIREX-AQ campaign. N is sample number measured for each condition. Each box-whisker presents the 5th, 25th, 50th, 75th and 95th percentile of sample values in each group.

ated using the synergistic measurement of HONO, NO and NO_2 concentrations in the field.

2 Methodology

2.1 Description of mobile laboratory platforms: Molab and MACH-2

During the WE-CAN campaign in August 2018, we conducted our measurements and sampling using the NOAA Chemical Science Division mobile laboratory (Molab), which was a cargo van with all instruments mounted on it. Meteorological instrumentation on the roof of the Molab provides temperature, relative humidity, wind speed, wind direction, altitude and GPS coordinates. All additional instruments were mounted onto the interior floor, and ambient air is sampled through 1 or 2 m Teflon inlets that exit the roof of the Molab via boreholes. NO and NO_x concentrations were measured with a Thermo Scientific Model 42i chemiluminescence NO / NO_x analyzer owned by Brown University, with ± 0.4 ppbv precision and 0.2 ppbv zero noise at 1 min time resolution. Note the NO_x concentration measured using the chemiluminescence analyzer can be falsely elevated due to known interferences from NO_y species, e.g., HONO and PAN. However, these data provide an upper limit of NO_x level that supports the isotopic collections of NO_x, HONO and nitrate. HONO and HNO_3 concentrations were measured using the University of New Hampshire's dual mist chamber and ion chromatograph (MC/IC) system with an uncertainty of 3 % at 5 min resolution (Chai et al., 2019; Scheuer et al., 2003). During the FIREX-AQ field campaign in July–August 2019, we mounted our sampling instruments onto the NASA Langley mobile aerosol characterization platform (MACH-2) (Kaspari et al., 2021).

2.2 Description of sampling location and strategy

While our sampling strategy was similar in both years, the actual sampling approach differed in response to fire condition and accessibility to fresh smoke from the mobile platforms.

During the 2018 WE-CAN campaign, our ground measurements and sampling targeted smoke from Rabbit Foot (RF) fire in the Challis area of Salmon–Challis National Forest in central Idaho, from 9 to 18 August 2018 (Salmon-Challis National Forest, 2018). Measurements were made at various locations around the Challis area of Idaho impacted by the RF fire, consisting of five different conditions: young smoke during nighttime (YN), young smoke during daytime (YD), aged smoke during nighttime (AN), aged smoke during daytime (AD) and mixed daytime smoke (M) that contains smoke contributed by either night smoke or fresh smoke. To sample the young smoke, we drove the Molab to Morgan Creek Road (MCR), which extends into a valley that was several kilometers away from the edge of the fire. We observed heavy smoke that based on distance and wind speed was expected to transport from the RF fire burning locations to the valley within a few hours or less. Three night trips and two day trips were made to MCR. While the nighttime measurements were conducted while driving, the daytime work was carried out while parked at a spike camp (i.e., a campsite for firefighters and support personnel) at the upper end of MCR; the spike camp was about 2 km from the fire, which we were able to see while conducting the measurements. The aged smoke was sampled at three stationary sites located around the Challis area, each less than 30 km away from the RF fire. All of these sites were recreational vehicle parks that allowed for power plugins. A total of 7 nights and 4 d were measured. The sampling locations and driving map are shown in Fig. S1 with detailed information on the measurements listed in Table 1.

During 2019 FIREX-AQ, we investigated five wildfires in the western US including Shady fire (Idaho), Black Diamond fire (Montana), Williams Flats fire (Washington), Nethker fire (Idaho) and Little Bear fire (Utah) from 24 July to 22 August 2019. We intensively sampled the emissions from Williams Flats fire and Nethker fire based on the large size and easy access to sampling locations (Fig. S2). Similar to

Table 1. Sampling condition and isotopic composition and concentration results for NO_x and HONO for Rabbit Foot (RF) fire during the 2018 WE-CAN campaign **(a)**, as well as Williams Flats (WF) fire and Nethker fire during the 2019 FIREX-AQ campaign **(b)**. Smoke conditions include young nighttime smoke (YN), young daytime smoke (YD), mixed daytime smoke (MD), aged nighttime smoke (AN) and aged daytime smoke (AD). The conditions are determined primarily by comparing the field data with the lab data involving three factors: δ^{18}O-HONO, δ^{15}N relationship between HONO and NO_x, and HONO / NO_x (or HONO / NO_2) ratio, along with the smoke sampling locations. Specifically, significantly elevated δ^{18}O-HONO indicates secondary production of HONO. Note that during the 2019 campaign, NO_x concentrations were not measured due to instrumental breakdown.

(a)

Start time (MDT)	End time (MDT)	Fire (smoke condition)	δ^{18}O-HONO	δ^{15}N-HONO	δ^{15}N-NO_x	[HONO] ppbv	[NO_x] ppbv	[NO_2] ppbv	HONO / NO_2	HONO / NO_x
08/09/18 10:11	08/09/18 19:10	RF (AD)	50.2‰	3.8‰	1.3‰	0.06	1.8	1.42	0.04	0.03
08/09/18 21:51	08/10/18 08:29	RF (AN)	37.3‰	−5.0‰	−2.5‰	0.06	1.3	1.35	0.04	0.05
08/10/18 09:50	08/10/18 20:26	RF (AD)	61.4‰	−1.7‰	−3.6‰	0.20	1.5	1.30	0.16	0.13
08/10/18 20:31	08/11/18 08:08	RF (AN)	60.4‰	−4.6‰	−2.9‰	0.15	1.4	1.39	0.11	0.11
08/11/18 22:43	08/12/18 09:38	RF (AN)	51.8‰	−5.8‰	−3.5‰	0.09	1.1	1.07	0.09	0.08
08/12/18 21:25	08/13/18 03:33	RF (AN)	62.1‰	−3.9‰	−2.6‰	0.26	0.8	0.81	0.33	0.33
08/13/18 03:53	08/13/18 07:05	RF (YN)	16.4‰	7.4‰	8.7‰	0.92	1.9	1.59	0.58	0.48
08/14/18 04:11	08/14/18 06:12	RF (YN)	16.1‰	−0.4‰	1.3‰	0.18	1.7	1.62	0.11	0.11
08/14/18 10:38	08/14/18 17:18	RF (AD)	57.0‰	1.6‰	−4.3‰	0.24	1.8	1.56	0.16	0.13
08/14/18 17:22	08/14/18 22:11	RF (AD)	78.0‰	3.8‰	−2.6‰	0.05	1.5	1.44	0.03	0.03
08/15/18 00:08	08/15/18 04:36	RF (YN)	9.8‰	1.1‰	2.0‰	0.98	5.5	4.90	0.20	0.18
08/15/18 05:52	08/15/18 07:12	RF (YN)	13.9‰	3.0‰	3.7‰	1.99	11.7	10.70	0.19	0.17
08/15/18 19:59	08/16/18 09:19	RF (AN)	41.6‰	−2.2‰	−1.5‰	0.15	5.9	5.78	0.03	0.03
08/16/18 15:56	08/16/18 17:51	RF (AD)	62.2‰	−2.7‰	−4.3‰	0.39	6.5	6.03	0.07	0.06
08/16/18 21:22	08/17/18 06:25	RF (AN)	59.0‰	−6.7‰	2.0‰	0.42	15.6	15.34	0.03	0.03
08/17/18 08:28	08/17/18 10:31	RF (M)	51.7‰	−6.0‰	−2.6‰	0.44	13.5	11.40	0.04	0.03
08/17/18 21:55	08/18/18 09:12	RF (AN)	63.5‰	−6.6‰	−1.1‰	0.25	12.3	12.15	0.02	0.02

(b)

Start time (MDT)	End time (MDT)	Fire (smoke condition)	δ^{18}O-HONO	δ^{15}N-HONO	δ^{15}N-NO_x	[HONO] ppbv	[NO_2] ppbv	HONO / NO_2
08/03/19 23:15:57	08/04/19 07:27:02	WF (AN)	44.6‰	−4.5‰	−3.9‰	0.31	5.7	0.05
08/04/19 18:25:49	08/05/19 09:40:08	WF (AN)	49.7‰	−6.3‰	−4.3‰	0.04	0.8	0.05
08/06/19 00:20:11	08/06/19 09:40:38	WF (YN)	16.3‰	−0.3‰	1.8‰	0.37	0.7	0.49
08/06/19 14:11:24	08/06/19 23:02:12	WF (M)	54.7‰	−6.1‰	−3.3‰	0.60	4.0	0.15
08/06/19 23:47:43	08/07/19 09:44:16	WF (YN)	32.3‰	2.2‰	2.9‰	0.18	2.2	0.08
08/09/19 12:32:42	08/09/19 14:56:34	Nethker (YD)	25.6‰	3.4‰	3.5‰	2.49	20.4	0.12
08/10/19 21:07:49	08/11/19 01:47:41	Nethker (YN)	25.1‰	2.2‰	1.8‰	1.23	2.3	0.54
08/12/19 03:24:15	08/12/19 11:24:47	Nethker (YN)	25.0‰	−0.6‰	0.1‰	1.69	3.5	0.48
08/13/19 21:38:03	08/14/19 01:28:27	Nethker (YN)	4.8‰	5.3‰	5.2‰	0.85	4.1	0.21
08/15/19 20:05:55	08/15/19 22:43:35	Nethker (AN)	34.3‰	−4.8‰	−0.8‰	1.01	3.4	0.30
08/15/19 22:57:07	08/16/19 06:28:04	Nethker (YN)	19.2‰	0.7‰	2.1‰	0.85	1.3	0.64

the 2018 field campaign, the measurements were conducted under YN, YD, AN, AD and M conditions.

2.3 Collection of HONO, NO_x and nitrate for isotopic analysis

Nitrogen oxides ($NO_x = NO + NO_2$), nitrous acid (HONO), particulate nitrate (p-NO_3^-) and nitric acid (HNO_3) were captured in the field using recently developed methods and sent to Brown University for analyses of isotopic composition (Chai et al., 2019; Fibiger and Hastings, 2016; Chai and Hastings, 2018; Fibiger et al., 2014). In brief, HONO was completely captured at a pumping flow rate of $\sim 10\,L\,min^{-1}$ with an annular denuder system (ADS), comprised (in order) of a Teflon particulate filter to remove p-NO_3^- and a Nylasorb filter to remove HNO_3, followed by two annular denuders, each coated with a premixed Na_2CO_3−glycerol−methanol−H_2O solution following a standard Environmental Protection Agency (EPA) method (Chai and Hastings, 2018). Within 24 h after each collection, the coating was extracted in 10 mL of ultrapure water (18.2 MΩ) in two sequential 5 mL extractions. Particulate nitrate on the upstream Millipore filters and HNO_3 from the Nylasorb filters, if there was any, were extracted by sonicating the filters in ∼ 30 mL ultrapure H_2O (18.2 MΩ). Samples with [NO_3^-] > 1 µM were analyzed for isotopic composition (concentration techniques detailed below).

The denuder-extracted solution with a pH of ∼ 10 was frozen and transported to Brown University for concentration and isotopic analysis, which was completed within 2 months

after the sampling. The timescales for sample extraction and isotopic analysis preserve both the solution concentration and isotopic composition of HONO in the form of nitrite (Chai and Hastings, 2018). The two-denuder setup allows for the minimization of the interference for both concentration and isotopic analysis from other N-containing species that could be trapped and form nitrite in residual amounts on the denuders, especially NO_2. Note that HONO levels were above the minimum detection limit (0.07 µM in extraction solution) and that the breakthrough amount of HONO threshold is far from being reached given the concentrations (Table 1), flow rate ($\sim 8\,L\,min^{-1}$) and collection times. Isotopic analysis of nitrite required the collection of a minimum amount of 10 nmol. NO_x was completely collected in an impinging solution containing 0.25 M $KMnO_4$ and 0.5 M NaOH which oxidizes NO and NO_2 to NO_3^- by pumping sampled air through a gas washing bottle at a flow rate of $\sim 4\,L\,min^{-1}$. Collection time for HONO ranged from 2 to 12 h and that for NO_x ranged from 0.75 to 2.5 h depending on their mixing ratios to make sure sufficient samples were captured against blanks for isotopic analysis (Fibiger et al., 2014; Fibiger and Hastings, 2016; Wojtal et al., 2016). Particulate filters and Nylasorb filters were collected over 7–12 h due to the low concentration of particulate nitrate and HNO_3.

The samples from each collection system were retrieved and processed following the procedures described in Chai et al. (2019). All treated samples from NO_x, HONO, p-NO_3^- and HNO_3 collection and their corresponding blanks were analyzed offline for concentrations of NO_2^- and NO_3^- with a WestCo SmartChem 200 discrete analyzer colorimetric system. The reproducibility of the concentration measurements was $\pm 0.3\,\mu mol\,L^{-1}$ (1σ) for NO_2^- and $\pm 0.4\,\mu mol\,L^{-1}$ for NO_3^- when a sample was repeatedly measured ($n = 30$). A detection limit of $0.07\,\mu mol\,L^{-1}$ for NO_2^- and $0.1\,\mu mol\,L^{-1}$ for NO_3^- was determined, and no detectable nitrite or nitrate was found in the blank denuder coating solution, whereas blank NO_3^- concentrations of ~ 5 µM are typical for the NO_x collection method (Fibiger et al., 2014; Wojtal et al., 2016). We only report the samples whose concentrations were at least 30 % above NO_3^- present in the blank $KMnO_4$ solution upon purchase to avoid increasing the error associated with the isotopic composition (Fibiger et al., 2014). Note that NO_3^- concentration was measured on the ADS solutions to verify whether and to what extent NO_2^- was oxidized to NO_3^- on denuder walls because the denitrifier method will convert both NO_3^- and NO_2^- to N_2O for isotopic analysis (see below).

Note that the complete collection of HONO and NO_x have been verified in various environments including biomass burning emissions. During the FIREX fire lab experiment, we applied the same method to quantify the HONO and NO_x isotopic composition (Chai et al., 2019). The concentrations of HONO captured with our ADS compared well with four other high-time-resolution concentration measurement techniques, including mist chamber and ion chromatography (MC/IC), open-path Fourier transform infrared spectroscopy, cavity-enhanced spectroscopy, and proton-transfer-reaction time-of-flight mass spectrometer. In the same work, the NO_x concentrations collected in the permanganate impinger were verified by real-time measurement with a chemiluminescence NO_x analyzer. In addition, our NO_x collection technique has been verified with real-time NO_x concentrations in on-road, near-road and urban background environments (Wojtal et al., 2016; Miller et al., 2017). These agreements verify complete capture of HONO and NO_x associated with biomass burning emissions using our techniques, which preserve the isotopic signatures without isotopic fractionation during the sampling process.

2.4 Isotopic analysis

The denitrifier method was used to complete nitrogen (^{15}N / ^{14}N) and oxygen (^{18}O / ^{16}O) isotope analyses of separate NO_3^- samples converted from NO_x and NO_2^- samples converted from HONO by quantitative conversion to N_2O by denitrifying bacteria *P. aureofaciens* (Casciotti et al., 2002; Sigman et al., 2001). The isotopic composition of N_2O is then determined by a Thermo Finnigan Delta V Plus isotope ratio mass spectrometer at m/z 44, 45 and 46 for $^{14}N^{14}N^{16}O$, $^{14}N^{15}N^{16}O$ and $^{14}N^{14}N^{18}O$, respectively. Sample analyses were corrected against replicate measurements of the NO_3^- isotopic reference materials USGS34, USGS35 and IAEA-NO-3 (Böhlke et al., 2003) and that of the NO_2^- isotopic reference materials N7373 and N10219. Precisions for δ^{15}N-NO_x, δ^{15}N-HONO and δ^{18}O-HONO isotopic analysis across each of the entire methods are ± 1.3 ‰, ± 0.6 ‰ and ± 0.5 ‰, respectively (Chai and Hastings, 2018; Fibiger et al., 2014).

3 Results and discussion

3.1 Concentrations of HONO and NO_x

Among the three fires, increased HONO concentrations were observed in young smoke during both night (0.2–2.0 ppbv) and day (2.5 ppbv), while HONO level is significantly lower in aged smoke during both night (0.06–1.0 ppbv) and day (0.05–0.6 ppbv) as shown in Fig. 2a. Although median values show young night and day are significantly higher than aged smoke day and night, there is significant overlap between young nighttime and aged day and night for WF and Nethker fires. These parts per billion volume to sub-parts per billion volume HONO concentrations can be a major OH source in areas that are impacted by wildfire. We also determined the molar ratio HONO / NO_2 from the concentrations for each sample (Fig. 3), and the values represent the upper bound of [HONO] / [NO_x] (Table 1a). Median ratios of [HONO] / [NO_2] for the five smoke conditions are 0.35 (YN), 0.12 (YD), 0.07 (AN), 0.09 (AD) and 0.04 (MD). The median ratios of [HONO] / [NO_2] for the young smoke fall in the range of fresh emissions measured in the lab (0.13–

0.53) and the field (0.05–0.33) (Yokelson et al., 2009; Selimovic et al., 2020, and references therein). Our results for YN are also in agreement with airborne measurements (0.34 ± 0.08) from the BB-Flux campaign that occurred in parallel with WE-CAN but are lower than the WE-CAN airborne observation of 0.72 ± 0.34 during the day (Theys et al., 2020; Peng et al., 2020). It is worth noting that the majority of the WE-CAN airborne data overlap with the BB-Flux results and our measurements, and Peng et al. (2020) associate very high ratios with different transport dynamics of fresh plumes. The concentration results for the ADS collected [HONO] agree well with that measured via MC/IC in real time and averaged over the ADS sampling periods (Fig. S3). The good agreement between these techniques sampling the same plumes near the ground and previous agreement with other HONO and NO_x observation methods suggest the concentrations are accurate (see also Sect. 2.3). It is important to also consider possible interference of peroxyacetyl nitrate (PAN) with NO_x collected in the alkaline permanganate solution for biomass burning conditions (Jaffe and Briggs, 2012). There is minimum PAN formed in fresh biomass burning (BB) emissions and young smoke of less than half an hour, based upon previous lab and field measurements, as well as modeling studies (Stockwell et al., 2014; Yokelson et al., 2009; Alvarado et al., 2010, 2015). In aged BB plumes in the upper troposphere, PAN can form rapidly at low temperatures and act as a temporary NO_x reservoir, reaching a maximum PAN / NO_y ratio of 0.3 (comparable to NO_x / NO_y) within ~ 2 to 4 h of aging after emission (Yokelson et al., 2009; Liu et al., 2016; Akagi et al., 2012). Though we note that these results are all from airborne measurements. There are no ground-level measurements for PAN in BB plumes during WE-CAN or FIREX-AQ, nor from other field studies to the best of our knowledge. PAN is thermally unstable in the boundary layer during summertime, and its main loss process in the atmosphere is thermal decomposition to release NO_2. The lifetime of PAN is on the order of 1 h or less at 20 °C and above (Talukdar et al., 1995; Fischer et al., 2010). We therefore expected PAN in near-ground air to maintain low levels or less due to photochemistry and thermal decomposition. Thus, given the short lifetime and the sample integration time of over 40 min to 2 h timescale, PAN is unlikely to interfere with our NO_x results.

In the aged smoke, [HONO] / [NO_2] are greatly reduced to median values of 0.05 and 0.07 observed for AN and AD, respectively, lower than the lab-derived range (Fig. 3). Wildfire plumes near ground level are expected to be more diluted than those directly injected upwards during the day, and the loss of HONO due to photolysis in the plume and/or surface reactions would be expected to be much faster than that in higher altitude dense plumes. The very low ratios indicate that HONO was lost faster than NO_x; however, given the 10–20 min lifetime of HONO against photolysis during the day and up to a couple of hours during the night (Nie et al., 2015), and considering aged smoke was sampled tens of kilometers from the fire, HONO levels may be maintained via secondary chemistry due to the high particle loadings and other terrestrial surface reactions in wildfire plumes (Alvarado and Prinn, 2009). While the concentration data are valuable for the ground-based setting near the fires, considerable uncertainty exists in the rate coefficients of the heterogeneous processes in daytime, as well as the HONO and NO_2 uptake coefficient and surface area densities (Appendix A). This makes it challenging to quantify the relative contribution of each potential pathway to the observed HONO budget.

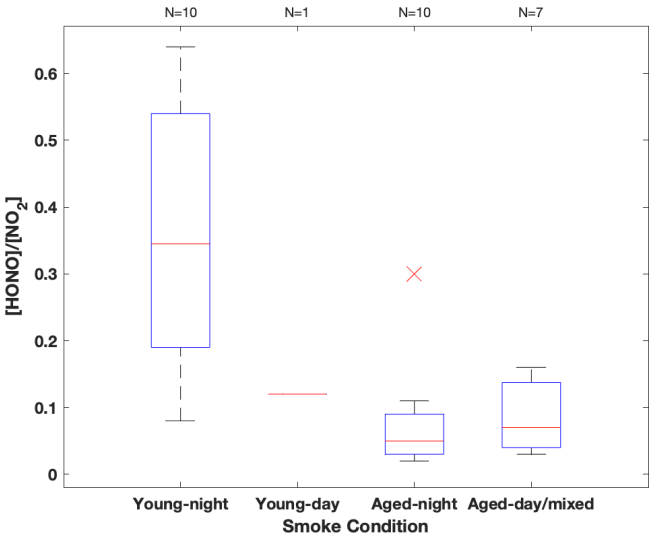

Figure 3. HONO / NO_2 concentration ratio summarized in box-whisker plot for each sampling condition. The red cross indicates an outlier. The whiskers from bottom to top represent 5 %, 25 %, 50 %, 75 % and 95 % quartiles.

3.2 Isotopic signatures of HONO and NO_x

In the 2016 FIREX fire laboratory experiment, we obtained δ^{15}N of NO_x and HONO, as well as δ^{18}O of HONO, in direct emissions from controlled burning of various vegetation biomasses representative of the western US (Chai et al., 2019). The lab-based δ^{15}N and δ^{18}O results serve as source signatures of biomass burning (BB) emissions: δ^{15}N-NO_x (-4.3 ‰ to $+7.0$ ‰) and δ^{15}N-HONO (-5.3 ‰ to $+5.8$ ‰) are derived from biomass N and the transformation in the combustion process, and δ^{18}O-HONO (5.2 ‰ to 15.2 ‰) incorporates δ^{18}O of molecular oxygen and water via combustion reactions (Chai et al., 2019). In the field, we expect that once NO_x and HONO are released and transported, atmospheric processing including photochemistry and nighttime chemistry would cause the isotopic composition of emitted NO_x and HONO to change.

By directly comparing the field-measured δ^{18}O-HONO with that measured from lab-controlled burning, we separate the data observed in young smoke from those in aged smoke. Very young smoke largely reflects fresh wildfire

emissions without significant atmospheric processing, while aged smoke δ^{18}O-HONO should deviate from the lab values due to the influence of secondary chemistry involving RN cycling. The δ^{18}O-HONO of young nighttime smoke ranged from 4.8 ‰ to 32.3 ‰ with a median value of 19.0 ‰, while the value in a single young daytime sample was 25.6 ‰ (Fig. 2b). There is a major overlap between the lab results and young nighttime smoke but with some higher δ^{18}O-HONO values in the field observations. These results suggest the HONO sampled in young smoke was dominated by primary BB emissions from the nearby wildfire but included contributions of secondarily produced HONO. By contrast, δ^{18}O-HONO is greatly elevated in aged smoke from all three fires both day and night. In addition, two aged smoke samples are labeled as mixed smoke because the collection interval included both sunlit and dark periods. The enrichment of δ^{18}O-HONO (up to 78 ‰), regardless of location and time, suggests that HONO in these conditions is produced by secondary chemistry involving NO, NO_2 and nitrate, which transfer high δ^{18}O values due to O_3 influence via photochemistry (Appendix B) (Thiemens, 2006; Michalski et al., 2003). The varying δ^{18}O-HONO values reflect different oxidizing environments, i.e., NO-to-NO_2 conversion via RO_2 versus O_3. These branching ratios can be determined if we resolve the dominant pathways for HONO production.

The δ^{15}N-HONO in the young smoke ranges from −0.3 ‰ to +7.4 ‰ with a median value of 2.8 ‰ for YN and +3.4 ‰ for YD, whereas that in the aged smoke shows decreased median values of −2.9 ‰ and −1.8 ‰ for AN and AD, respectively. In addition, the daytime aged smoke exhibits the largest variability (Fig. 2c), and this likely reflects daytime HONO secondary chemistry. It is noted that δ^{15}N-NO_x and δ^{15}N-HONO measured across the entire period of all three fires at ground level ranges from −4.3 ‰ to +8.7 ‰ and −6.7 ‰ to +7.4 ‰, respectively, with the majority overlapping with the corresponding ranges found in the fire laboratory experiment and no significant difference in mean values (p value >0.5) (Chai et al., 2019; Fibiger and Hastings, 2016). This consistency suggests δ^{15}N is a reliable tracker generally for BB-derived NO_x and HONO, although there is clear variability between the different smoke conditions that can refine our understanding of reactive N cycling. We note again that, although no near-ground PAN measurements in BB plumes are available, the isotopic results also suggest that PAN interference is not important to the δ^{15}N-NO_x results. For aged smoke, we would expect δ^{15}N-NO_x to decrease from that in fresh emissions due to partial transformation of NO_x to additional oxidized N products (e.g., PAN), as well as isotopic exchange between NO_x and these oxidized species; both processes will leave ^{15}N depleted in NO_x and ^{15}N enriched in PAN (Walters and Michalski, 2015). If PAN existed at significant concentrations that were (1) comparable with NO_x in the atmosphere and (2) completely collected in the permanganate solution, then the δ^{15}N would reflect the overall δ^{15}N of NO_x + PAN in the final reduced permanganate solution. In this case, we would expect that aged smoke would not shift from the δ^{15}N-NO_x range of young smoke because δ^{15}N shifts in both PAN and NO_x could offset each other. However, our observed δ^{15}N-NO_x mean values for both aged daytime and nighttime smoke are significantly (p <0.05) lower than that of the young smoke, a good indicator of a lack of PAN interference on the isotopic results (see also Miller et al., 2017).

Our prior lab-controlled burning study revealed a linear relationship between δ^{15}N-HONO and δ^{15}N-NO_x, with δ^{15}N-HONO slightly more negative than δ^{15}N-NO_x in fresh BB emissions (Chai et al., 2019). This δ^{15}N relationship is plotted as a solid line, together with all field observations, to illustrate the potential influence of atmospheric processing on the δ^{15}N-HONO and δ^{15}N-NO_x (Fig. 4). The plot can be sub-divided into three regimes. In regime I, we find all of the δ^{15}N of NO_x and HONO in young smoke from both daytime and nighttime. In this young smoke regime, more positive δ^{15}N than that of the rest of our samples is found for both species, and all samples concur with the δ^{15}N relationship found for fresh emissions (Fig. 4). This, along with the low δ^{18}O-HONO associated with these samples (Fig. 2b), confirms HONO is not significantly affected by secondary chemical processing in the air mass captured from fresh smoke. Regime II is filled with the results of daytime aged smoke ∼ 30 km away from the RF fire; these results exhibited much more positive δ^{15}N-HONO than δ^{15}N-NO_x by 3 ‰ to 6 ‰, as well as the largest (positive) discrepancy from the BB δ^{15}N relationship line, as shown in the upper left region of Fig. 4. The daytime aged smoke also exhibited the highest values of δ^{18}O-HONO observed (Fig. 2). All samples of aged nighttime smoke that were collected fall in regime III. While the majority of the regime III data fall within the 95 % confidence interval for the lab-based δ^{15}N relationship, there is a tendency for these samples to have δ^{15}N-HONO that was more negative than δ^{15}N-NO_x to different degrees of up to −8.7 ‰. In particular, we hypothesize that the combination of more negative δ^{15}N-HONO values and elevated δ^{18}O-HONO indicate secondary production of HONO. We next explore quantitative use of δ^{15}N-NO_x, δ^{15}N-HONO and δ^{18}O-HONO to understand the isotopic shifts in terms of secondary chemistry involving RN cycling.

3.3 Isotopic mass balance modeling

In aged smoke, the observed δ^{18}O-HONO enhancement and shift of δ^{15}N values away from the δ^{15}N NO_x–HONO line, as a result of RN cycling, would be expected to be derived from the integrated kinetic isotopic fractionation (expressed as enrichment factor $^{18}\varepsilon$ and $^{15}\varepsilon$) associated with each of the loss/production processes (Fig. 1) weighted by their relative contribution to the budget. By definition, $\varepsilon = (\alpha - 1) \times 1000$ ‰, with fractionation factor α referring to the rate coefficient ratio between the heavy isotopologue and the light isotopologue. For δ^{18}O-HONO, we also took into

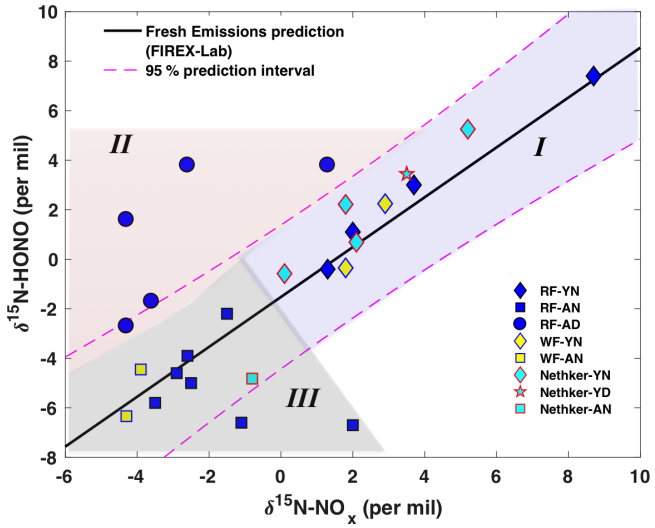

Figure 4. Relationship between wildfire-derived δ^{15}N-HONO and δ^{15}N-NO_x. Samples from plumes of three wildfires including Rabbit Foot fire (RF; 2018), Williams Flats fire (WF; 2019) and Nethker fire (2019) are shown as different colors. Different symbols indicate different smoke conditions including young nighttime smoke (YN), young daytime smoke (YD), aged nighttime smoke (AN) and aged daytime smoke (AD). Note that the mixed smoke samples displayed in Fig. 2 are not shown here due to their large uncertainty. The solid black line (δ^{15}N-HONO $= 1.01\delta^{15}$N-$NO_x - 1.52$; $R^2 = 0.89$, $p<0.001$) is derived from lab-controlled burning emissions during the 2016 FIREX fire lab study (Chai et al., 2019) and within the 95 % confidence interval (dashed magenta lines) predicts much of the field-based δ^{15}N-HONO versus δ^{15}N-NO_x. The field data are further grouped into three regimes – young smoke in both day and night (*I*, light purple shading), aged daytime smoke (*II*, pink shading) and aged nighttime smoke (*III*, gray shading) based upon the δ^{18}O-HONO results.

account the transferring effect of oxygen from different O-containing reactants that produce HONO (as explained in Appendix B). In order to elucidate the relative role each process plays in the HONO budget, we constructed an isotopic mass balance model for δ^{15}N and for δ^{18}O.

In aged smoke, a deviation in δ^{15}N, represented as $\Delta\delta^{15}N_{HONO-NO_x}$ ($= \delta^{15}$N-HONO $- \delta^{15}$N-NO_x), is simulated following Eq. (1), where f is the fraction of reaction i (reaction numbering in Sect. 1) to total loss (L) or production (P) of HONO. δ^{18}O-HONO is simulated following Eq. (2), in which the change in δ^{18}O-$HONO_{i,P}$ arises from, in addition to kinetic isotopic fractionation, the transferring of $\delta^{18}O_{i,t}$ (Eq. 3) in the reactant (OH, NO, NO_2, H_2O and NO_3^-) to the product HONO as HONO contains two O atoms that may stem from more than one reactant (Appendix B). The δ^{18}O values of all possible reactions that produce HONO are evaluated, as tabulated in Table S1 in the Supplement, to help determine δ^{18}O of NO, NO_2 and HONO. The isotopic enrichment factors $^{15}\varepsilon$ and $^{18}\varepsilon$ associated with each of Reactions (R1)–(R7) are computed via theoretical principles as none of these key parameters are currently available in the literature (Appendix B).

$$\Delta\delta^{15}N_{HONO-NO_x} = \sum_{i,L}\left(f_{i,L}\times\Delta\delta^{15}N_{i,L}\right) + \sum_{i,P}\left(f_{i,P}\times\Delta\delta^{15}N_{i,P}\right) \quad (1)$$

$$\delta^{18}O{-}HONO = \sum_{i,L}\left(f_{i,L}\times{}^{18}\varepsilon_{i,L}\right) + \sum_{i,P}\left(f_{i,P}\times\Delta\delta^{18}O{-}HONO_{i,P}\right) \quad (2)$$

$$\Delta\delta^{18}O - HONO_{i,P} = \delta^{18}O_{i,t} + {}^{18}\varepsilon_{i,P} \quad (3)$$

3.3.1 Modeling of δ^{15}N of HONO and NO_x in aged daytime and nighttime smoke

We first simulated $\Delta\delta^{15}N_{HONO-NO_x}$ for both daytime and nighttime aged conditions using this model. According to the potential HONO–NO_x chemistry in ground areas impacted by wildfire smoke plumes (Fig. 1), HONO is expected to be predominantly lost to photolysis (Reaction R1) during the day. It is well known that HONO can be produced via a gas-phase radical recombination reaction between NO and OH (Reaction R2) (Platt et al., 1980). However, the rate of Reaction (R2), calculated from the rate coefficient, the typical daytime OH concentration ($1–2\times10^6$ molecule cm^{-3}) (de Gouw et al., 2006) in biomass burning plumes and our measured mean NO_x concentration, can only account for up to 15 % of the HONO production rate (Appendix A and Table A1). Under a typical pseudo-steady-state approximation (PSSA) ($d[HONO]/dt \approx 0$), additional sources of HONO must be included to balance the HONO budget. Thus, we modeled three scenarios varying the relative contribution of Reaction (R2) as 5 %, 10 % and 15 %. With rapid photolytic loss, HONO has a lifetime nearly 2 orders of magnitude shorter than the lifetime of NO in Reaction (R2), as well as that of NO_2 in Reaction (R3) and nitrate in Reaction (R4); thus, the $\Delta\delta^{15}N_{HONO-NO_x}$ is mostly sensitive to the change in $\delta^{15}N_{HONO}$ immediately upon photolysis but overall remains constant, associated with Reactions (R2)–(R4) within the timescale of HONO photolysis. We quantify the remaining HONO fraction from secondary production, f_{rp}, to represent HONO that has been produced but not yet photolyzed. Thus, the daytime $\Delta\delta^{15}N_{HONO-NO_x}$ for aged smoke was simulated as a function of f_{rp} following a Rayleigh-type isotopic fractionation scheme (Fig. 5 and Sect. B2.1). Generally, $\Delta\delta^{15}N_{HONO-NO_x}$ follows an exponential increase as f_{rp} decreases. In other words, as more photolysis occurs the difference in the remaining δ^{15}N-HONO and the δ^{15}N-NO_x increases, and this is driven by the negative value of $^{15}\varepsilon_1$ which tends to enrich ^{15}N in the HONO reactant (Reaction R1). The simulation was carried out for two different sets of HONO production mechanisms, with HONO photolysis being the dominant loss pathway. With mechanism M1 (solid lines in Fig. 5), photo-induced surface NO_2-to-HONO conversion (Reaction R3) is the major pathway in

addition to gas-phase OH + NO (Reaction R2) to produce HONO. As $^{15}\varepsilon_2$ has a positive value, a larger Reaction (R2) contribution leads to higher $\Delta\delta^{15}N_{HONO-NO_x}$. With mechanism M2 (dashed line in Fig. 5), nitrate photolysis (Reaction R4) is included in addition to Reactions (R2) and (R3) in the HONO production mechanism. Taking the contribution of Reaction (R2) of 10 % as a constant, three scenarios were modeled by varying the relative contribution of Reaction (R3) (75 %–85 %) and Reaction (R4) (5 %–15 %). The results suggest larger Reaction (R4) contribution yields lower $\Delta\delta^{15}N_{HONO-NO_x}$ due to severe ^{15}N depletion associated with nitrate photolysis ($^{15}\varepsilon_4 \leq -47.9$ ‰) (Appendix B). Importantly, the addition of Reaction (R4) in M2 also lowers $\Delta\delta^{15}N_{HONO-NO_x}$ compared to M1. By applying the field-observed $\Delta\delta^{15}N_{HONO-NO_x}$ for the aged daytime smoke to the model, we solved f_{rp} for all scenarios and plotted these as circles in Fig. 5. All five aged daytime datasets from RF can be reproduced by M1 under all three scenarios; by contrast, via M2, none of the three scenarios can explain the two highest $\Delta\delta^{15}N_{HONO-NO_x}$ values observed in the field. As such, we conclude that Reaction (R4) plays a minor role (<5 %) in the secondary HONO production in the aged daytime smoke during our sampling periods. Rather, HONO forms primarily via Reactions (R2) and (R3) during the day in the areas impacted by aged wildfire smoke. However, there are two limitations to the modeling results. First, as the ^{15}N / ^{14}N fractionation associated with Reactions (R3), (R6) and (R7) are not distinguishable with our current parameterization (Appendix B1.2 and B2.2), we cannot rule out the potential importance of heterogeneous NO_2-to-HONO conversions (Reactions R6 and R7) in daytime. Second, it should be noted that the results represent our best estimate of the average relative importance of Reactions (R2)–(R4) for HONO production during our HONO sampling periods (2–10 h) for the aged daytime plume. Due to the long sample integration time, our samples were influenced by both aged smoke and near-background air when the smoke was very diluted. Under the NO_x-limited condition (low NO_x <1 ppbv) in remote background air, nitrate photolysis is expected to be the major secondary HONO source (Ye et al., 2016; Zhou et al., 2011), which cannot be ruled out by our results. Isotopic measurement techniques with higher time resolution will be required to achieve real-time quantification of the HONO budget.

For the nighttime smoke, we simulated that the HONO budget is maintained by Reactions (R5)–(R7). $\Delta\delta^{15}N_{HONO-NO_x}$ reflects the combination of kinetic isotopic fractionation $^{15}\varepsilon_5$ associated with the HONO loss (Reaction R5) and production reactions (Reactions R6 and R7 in proportion). With our calculated uptake $^{15}\varepsilon_5$ (−2 ‰) and estimated $^{15}\varepsilon_6$ or $^{15}\varepsilon_7$ (ranging from −2.9 ‰ to −4.5 ‰), we obtained $\Delta\delta^{15}N_{HONO-NO_x}$ ranging from −0.9 ‰ to −2.5 ‰ when uptake and production occur at a similar timescale (rate coefficient), and this can explain the majority of observed aged nighttime results (regime III; Fig. 4). Two aged nighttime points sampled for RF (16 and 17 August 2018) fall outside of the predicted range, with much lower $\Delta\delta^{15}N_{HONO-NO_x}$ (−8.7 ‰ and −5.5 ‰, respectively). These two samples were associated with 2–10 times elevated NO_x concentration compared to the previous 4 nights and likely higher concentrations of particulate matter (Figs. 2a; Fig. S4 in the Supplement). This could cause an accelerated conversion of NO_2-to-HONO, which is not accounted for in the steady state estimation above, leading to the much lower $\Delta\delta^{15}N_{HONO-NO_x}$ values that were observed.

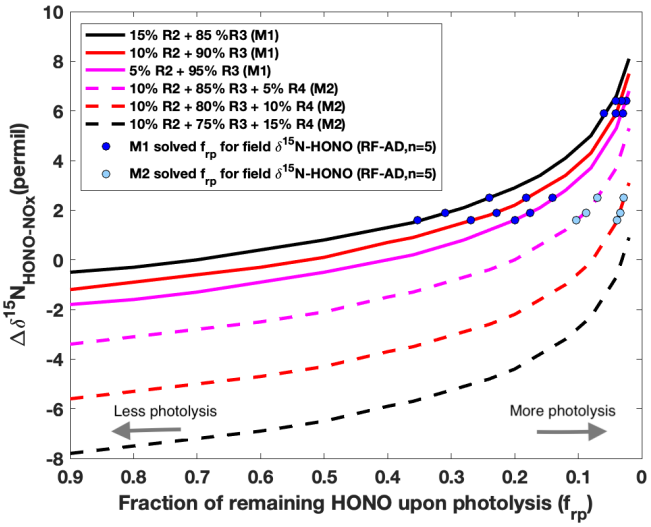

Figure 5. Modeling results of $\delta^{15}N$ for aged daytime smoke via two plausible mechanisms (M1 and M2) for secondary HONO production. The isotope mass balance model (Eq. 1) is used to simulate the $\delta^{15}N$ difference ($\Delta\delta^{15}N_{HONO-NO_x} = \delta^{15}N_{HONO} - \delta^{15}N_{NO_x}$) as a function of the fraction of HONO remaining after photolysis (f_{rp}) in a pseudo-photochemical steady state. The calculated kinetic fractionation factors used here are explained in Appendix B. In the first mechanism (M1, solid lines), Reaction (R3) is the major HONO production pathway with a varying relative contribution from Reaction (R2), which is constrained as producing no more than 15 % of the observed HONO concentrations. In the second mechanism (M2, dashed lines), nitrate photolysis (Reaction R4) is included in addition to Reactions (R2) and (R3) for HONO production. Taking the contribution of Reaction (R2) of 10 % as a constant, three scenarios were modeled by varying the relative contribution of Reaction (R3) (75 %–85 %) and (R4) (5 %–15 %).

3.3.2 Modeling of $\delta^{18}O$ of HONO in aged daytime and nighttime smoke

The $\delta^{18}O$-HONO of daytime aged smoke was modeled following M1 (Reactions R1–R3) derived based upon the $\delta^{15}N$ modeling results: NO and NO_2 are cycled via NO_2 photolysis and NO oxidation by O_3 and/or peroxy radicals (RO_2 including HO_2) during the day, through which $\delta^{18}O$ of O_3 and RO_2 can be passed to NO and NO_2 via mass transfer (Eqs. B10–B12). O_3 is known to have an intrinsically high $\delta^{18}O$ value of up to ∼ 117 ‰ caused by unique isotopic frac-

tionation associated with photochemical gas-phase O_3 formation (Thiemens, 2006), while OH and RO_2 have very low $\delta^{18}O$ values (Thiemens, 2006). O_3 participation in reactive N cycling involving NO_x (Reaction R8) results in high $\delta^{18}O$ of NO_2 (Michalski et al., 2003; Walters et al., 2018). In pseudo-photochemical steady state, NO and NO_2 are expected to have similar $\delta^{18}O$ which is a result of competition between O_3 and RO_2 oxidation (Reactions R8–R10), expressed as $f^{NO}_{O_3/(O_3+RO_2)}$ via Eqs. (4) and (5) below.

$$NO + O_3 \rightarrow NO_2 + O_2 \quad (R8)$$

$$NO + HO_2/RO_2 \rightarrow NO_2 + HO/RO \quad (R9a)$$

$$\rightarrow HONO_2/RONO_2\,(5\,\%) \quad (R9b)$$

$$NO_2 + h\nu + O_2 \rightarrow NO + O_3 \quad (R10)$$

$$\delta^{18}O{-}NO \approx \delta^{18}O{-}NO_2 = f^{NO}_{O_3/(O_3+RO_2)} \times \delta^{18}O{-}O_3 + \left(1 - f^{NO}_{O_3/(O_3+RO_2)}\right) \times \delta^{18}O{-}RO_2 \quad (4)$$

$$f^{NO}_{O_3/(O_3+RO_2)} = \frac{k_{NO+O_3}[O_3]}{k_{NO+O_3}[O_3] + k_{NO+RO_2}[RO_2]} \quad (5)$$

The $\delta^{18}O$ signature is subsequently passed to HONO when it is produced from NO (Reaction R2) and NO_2 (Reaction R3) during the day and from NO_2 (Reactions R6 and R7) during the night, and thus $\delta^{18}O$-HONO is a positive linear function of $f^{NO}_{O_3/(O_3+RO_2)}$ if kinetic isotopic fractionation ($^{18}\varepsilon$) associated with these processes are fixed values (as calculated in Appendix B). Given that HONO is predominantly produced via Reactions (R2) and (R3) in aged daytime smoke (Fig. 5), $\delta^{18}O$-HONO was simulated following the three M1 scenarios with the contribution of Reaction (R2) varying from 5 % to 15 %. All three scenarios reproduced the range of our field results for aged daytime smoke, further pointing to M1 as explaining the HONO in this environment. In addition, the variation in $\delta^{18}O$ was driven by differing oxidation that is determined by $f^{NO}_{O_3/(O_3+RO_2)}$, which depends on the relative concentration of O_3 to RO_2 (Figs. S5 and S6). The $f^{NO}_{O_3/(O_3+RO_2)}$ corresponding to each observed $\delta^{18}O$-HONO were solved and plotted in Fig. 6a. We found $f^{NO}_{O_3/(O_3+RO_2)}$ decreased by less than 0.02 as the contribution of Reaction (R2) to total HONO production decreased from 15 % to 5 %. On the other hand, $\delta^{18}O$-HONO changes sensitively with varying $f^{NO}_{O_3/(O_3+RO_2)}$, increasing from 50.2 ‰ to 78.0 ‰ as the fraction of NO oxidized by O_3 rather than RO_2 increases from 0.34 to 0.65.

The $\delta^{18}O$-HONO of nighttime aged smoke was modeled following the nighttime chemistry (Reactions R5–R7), i.e., taking NO_2 conversion as the source and surface uptake as the sink. In areas impacted by nighttime aged smoke, HONO forms from wildfire-derived NO_2 residing in the nocturnal boundary layer. As the two pathways (Reactions R6 and R7) for heterogeneous NO_2 conversion lead to very different $\delta^{18}O$-HONO stemming from different $\delta^{18}O$ transfer (Appendix B), we examined the relative importance of the two

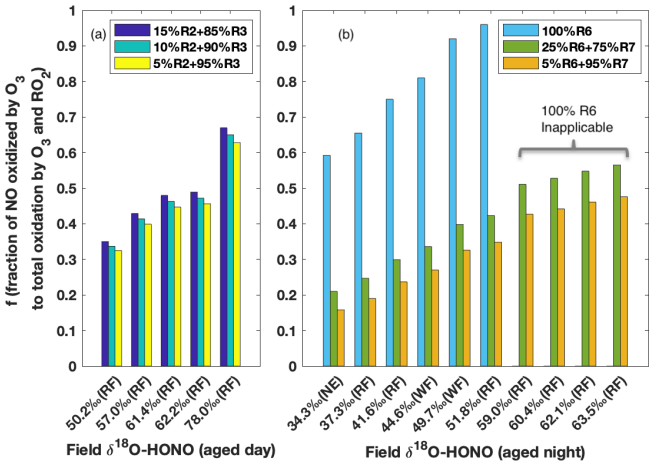

Figure 6. Model prediction of fraction of NO oxidized to NO_2 via O_3 to that via O_3 and RO_2 together ($f^{NO}_{O_3/(O_3+RO_2)}$) on the basis of field-measured $\delta^{18}O$-HONO for aged daytime **(a)** and nighttime **(b)** smoke. During the day **(a)**, the contribution of Reaction (R2) to HONO production is varied from 5 % to 15 % following M1 in Fig. 5, and Reaction (R3) accounts for the remaining secondary HONO contribution. The modeling results are shown in Fig. S5 and Table S3 in the Supplement. During the night **(b)**, three scenarios with various contributions of Reactions (R6) and (R7) are modeled (Fig. S6 and Table S4). $f^{NO}_{O_3/(O_3+RO_2)}$ is predicted to be over unity for the last four observed $\delta^{18}O$-HONO values if Reaction (R6) is assumed as the only nighttime pathway.

pathways for HONO production by varying the relative contribution between the two pathways and comparing it to the observed $\delta^{18}O$-HONO (Fig. 6b). If HONO is constrained to exclusively form via Reaction (R6) (surface hydrolysis), the model would require an unrealistic $f^{NO}_{O_3/(O_3+RO_2)} > 100\,\%$ to explain $\delta^{18}O$-HONO > 55 ‰. Even for samples with lower $\delta^{18}O$-HONO values (34 ‰ to 52 ‰), the high branching ratio $f^{NO}_{O_3/(O_3+RO_2)}$ (>0.6) required to create such large enrichment is unrealistic for BB environments. In particular, $[O_3]$ / $[RO_2]$ converted from $f^{NO}_{O_3/(O_3+RO_2)}$ solved under this mechanism is at least twice as large as values derived from the previous field measurement of aged wildfire smoke (Baylon et al., 2018). By contrast, the inclusion of Reaction (R7) in addition to Reaction (R6) in rate ratios 3 : 1 and 20 : 1 based on previous lab studies (Kebede et al., 2016; Scharko et al., 2017) can elevate the modeled $\delta^{18}O$-HONO and explain all observed $\delta^{18}O$-HONO values. This suggests NO_2-to-HONO heterogeneous conversion catalyzed by surface-hosted iron oxides and quinone (Reaction R7) in the nighttime aged smoke proceeds significantly faster than NO_2 hydrolysis (Reaction R6). Our isotopic analyses provide evidence for the participation of such a pathway in BB environments and also shows the capability to constrain the relative importance between these two pathways. Although the daytime $\delta^{18}O$-HONO can be larger than that of nighttime aged smoke, similar $[O_3]$ / $[RO_2]$ ratios are derived from our

solved $f^{NO}_{O_3/(O_3+RO_2)}$ and are consistent with the limited field measurements (Parrington et al., 2013; Baylon et al., 2018), and they further indicate the important role peroxy radicals play as an oxidant in wildfire-smoke-impacted environments.

4 Conclusions

As wildfire has enormously impacted climate, air quality and ecosystems in the past and is expected to worsen (Westerling, 2016), accurately tracking wildfire-derived reactive nitrogen species (i.e., NO_x and HONO) and their cycling is extremely important for quantifying and mitigating key pollutants such as O_3 in wildfire-impacted areas both close to the fire and thousands of kilometers downwind. We show δ^{15}N-HONO and δ^{15}N-NO_x can serve as a powerful tool to track BB sources and constrain secondary HONO production pathways. With the help of field-observed δ^{18}O-HONO, we grouped our measured relationship between the δ^{15}N-HONO and δ^{15}N-NO_x into three different regimes, which clearly distinguish between young wildfire plumes, aged daytime plumes and aged nighttime plumes. The δ^{15}N results allow for constraining the daytime HONO budget and particularly secondary production mechanisms via the isotope mass balance simulation. The use of excess δ^{15}N ($\Delta\delta^{15}N_{HONO-NO_x}$) also provides an approach for constraining HONO budgets in other environmental settings, such as urban ambient areas and remote areas including forest and polar regions. Furthermore, by combining δ^{15}N emission source signatures and chemical fractionation characteristics, we could potentially track the impact and relative role of wildfire-derived reactive nitrogen more extensively when the plume transfers thousands of kilometers downwind and mixes with other air such as urban plumes. In addition, the δ^{18}O-HONO results not only offer direct evidence for secondary production of HONO that allows for the determination of the NO oxidizing branching ratio between O_3 and RO_2 but also constrains nighttime HONO production mechanisms. We expect to apply the δ^{18}O-HONO approach to a variety of atmospheric settings for constraining the HONO budget and its cycling with other reactive nitrogen species, as well as O_3. As such, online isotopic measurement techniques with higher time resolution will benefit the use of stable isotopes and broaden its application in atmospheric chemistry. In the meantime, in order to more accurately quantify the relative contribution of these potential pathways, further experimental and theoretical investigations on isotopic fractionation characteristics of each pathway under various environmental conditions are required.

Appendix A: Overview of HONO budget quantification under different conditions based upon concentrations

A common approach to quantitatively understand the wildfire-derived HONO budget – its direct emissions, secondary productions and sinks – is to use concentration-based mass balance calculation. Ideally, if we know the rate coefficients and reactant concentrations for each of the pathways, we would be able to quantify the relative contribution of each pathway to the total HONO concentration measured in the field under the assumption of pseudo-steady-state approximation (PSSA) as described in Eq. (A1), where R_{emission}, $R_{\text{production}}$ and R_{loss} are rate of emission, production and loss, respectively. In aged smoke, we expect HONO is almost exclusively produced from secondary formation. During the day, HONO is predominantly lost to photolysis with a coefficient depending on solar zenith angle differing with time of the day, while one or more reactions of Reactions (R2)–(R4) may be responsible for producing HONO. Under PSSA, using the well quantified rate coefficient k_2, observed NO and HONO concentrations, estimated OH concentration, and TUV-model-calculated (tropospheric ultraviolet and visible) HONO photolysis coefficient j_{HONO}, we estimated the ratio of Reaction (R2) to the total HONO production ($P_{\text{OH+NO}}$) via Eq. (A2) and found Reaction (R2) can only contribute 2 %–15 % (Table A1) of the total HONO production under the ambient conditions when the five aged daytime samples were collected. This suggests at least 85 % of HONO was produced from heterogeneous HONO formation via Reaction (R3) and/or Reaction (R4).

$$\frac{\mathrm{d[HONO]}}{\mathrm{d}t} = R_{\text{emission}} + R_{\text{production}} - R_{\text{loss}} \approx 0 \quad \text{(A1)}$$

$$P_{\text{OH+NO}} = \frac{k_2\,[\text{OH}]\,[\text{NO}]}{j_{\text{HONO}}[\text{HONO}]} \quad \text{(A2)}$$

HONO production from photo-enhanced NO_2 conversion has been proposed to take place on various types of surfaces. However, the uptake coefficient ($\gamma^{h\nu}_{\text{NO}_2\rightarrow\text{HONO}}$), which indicates the probability of NO_2 collisions with a surface that results in the formation of a HONO molecule, varies by at least 3 orders of magnitude depending on the specific type of surface materials. For instance, $\gamma^{h\nu}_{\text{NO}_2\rightarrow\text{HONO}}$ on soot particles was found to range from 3.7×10^{-4} to 1.1×10^{-3} s^{-1} (Ammann et al., 1998), while that on surfaces comprised of humic acid was measured as $2\text{–}8\times10^{-5}$ s^{-1} in several lab studies (Stemmler et al., 2006; Scharko et al., 2017). The latter is consistent with daytime modeling results of 6×10^{-5} s^{-1} (Wong et al., 2013). Additionally, a much smaller (10^{-7}–10^{-6} s^{-1}) $\gamma^{h\nu}_{\text{NO}_2\rightarrow\text{HONO}}$ value was obtained for metal oxide surfaces such as TiO_2 and SiO_2 (Ndour et al., 2008).

Daytime photolysis of nitrate (HNO_3 and pNO_3^-) via Reaction (R4) has also been proposed as an important renoxification pathway that produces HONO and NO_2 in low NO_x remote environments (Zhou et al., 2011), as well as high NO_x urban settings with abundant urban grime (Baergen and Donaldson, 2016, 2013). The p-NO_3^- and surface-adsorbed HNO_3 were found to be photolyzed with rate coefficients 2–3 orders of magnitude larger than gas-phase HNO_3 and possess lifetimes as short as a few hours (Ye et al., 2017). However, the rate coefficient of Reaction (R4) is poorly constrained. Not only have the branching ratios between the NO_x-producing channel and HONO-forming channel been poorly known (Baergen and Donaldson, 2016), but previous laboratory-measured nitrate photolysis rate coefficients also vary by up to 3 orders of magnitude (Ye et al., 2017). The uncertainty is even greater because it is complicated by dependence on relative humidity, particle composition and pH.

During the night, HONO is primarily lost to uptake on surfaces including aerosols and soils, and the uptake coefficient can be expressed by Eq. (A3).

$$L^{\text{uptake}}_{\text{HONO}} = 0.25 \times \gamma_{\text{HONO}} \times \overline{\omega_{\text{HONO}}} \times S/V \times 100 \quad \text{(A3)}$$

In this equation, $\overline{\omega_{\text{HONO}}}$ is the mean thermal HONO molecular velocity calculated by $\overline{\omega_{\text{HONO}}} = \sqrt{8RT/\pi M}$, where R, T and M are the gas constant, absolute temperature and molecular weight. S/V is the surface-to-volume ratio (cm^2 cm^{-3}). The uptake coefficient γ_{HONO} was measured to be 10^{-5} for soil surface and in the range of 10^{-5}–10^{-3} for aerosol particle surface (Donaldson et al., 2014b; Wong et al., 2012). In addition, OH + HONO occurs at rates 1–2 orders of magnitude smaller than the uptake and therefore plays a minor role. The combined loss processes lead to a HONO lifetime of about 4 h during the night.

HONO is generally assumed to be produced via heterogeneous NO_2 hydrolysis disproportionation (Reaction R6) (Finlayson-Pitts et al., 2003), and the production rate of HONO is estimated by Eq. (A4), expressed in the unit of ppbv-HONO ppbv^{-1}-NO_2 s^{-1}.

$$\begin{aligned} P^{\text{night}}_{\text{HONO}} &= 0.5 \times R^{\text{surface}}_{\text{NO}_2\rightarrow\text{HONO}} \\ &= 0.5 \times \gamma_{\text{NO}_2} \times \overline{\omega_{\text{NO}_2}} \times S/V \times 100, \end{aligned} \quad \text{(A4)}$$

where $\overline{\omega_{\text{NO}_2}}$ is the mean NO_2 molecular velocity, and S/V is the surface-to-volume ratio of particles, which could range from 9.0×10^{-6} to 3.0×10^{-4} cm^2 cm^{-3} for normally polluted areas and highly polluted areas, respectively (Spataro and Ianniello, 2014). The S/V in biomass burning smoke plumes has huge uncertainty; additionally, ground surface is also expected to play an important role in nighttime HONO production given our ground sampling location (Tuite et al., 2021; Scharko et al., 2017; Kebede et al., 2016; Stemmler et al., 2006); however, its S/V is not well defined/quantified.

Overall, considerable uncertainty remains regarding the rate coefficient of the heterogeneous processes in the daytime, as well as the HONO and NO_2 uptake coefficients and S/V ratio. This uncertainty, complicated further with large variability in fire behavior and emissions, make the HONO budget quantification extremely challenging.

Table A1. HONO budget estimation.

						$[OH] = 1 \times 10^6$ molecule cm^{-3}		$[OH] = 2 \times 10^6$ molecule cm^{-3}	
Start time (MDT)	Stop time (MDT)	[HONO] ppbv	[NO] ppbv	[NO_2] ppbv	j_{HONO} s^{-1}	k[OH] s^{-1}	P_{OH+NO}/L_{HONO}	k[OH] s^{-1}	P_{OH+NO}/L_{HONO}
08/16/18 15:56	08/16/18 17:51	0.39	0.51	6.03	1.2×10^{-3}	1.2×10^{-5}	0.01	2.4×10^{-5}	0.03
08/09/18 15:38	08/09/18 19:10	0.06	0.41	1.42	1.1×10^{-3}	1.2×10^{-5}	0.08	2.4×10^{-5}	0.15
08/14/18 10:38	08/14/18 17:18	0.24	0.22	1.56	1.4×10^{-3}	1.2×10^{-5}	0.01	2.4×10^{-5}	0.02
08/14/18 17:22	08/14/18 20:11	0.05	0.07	1.44	6.1×10^{-3}	1.2×10^{-5}	0.03	2.4×10^{-5}	0.06
08/10/18 09:50	08/10/18 20:26	0.20	0.22	1.30	1.1×10^{-3}	1.2×10^{-5}	0.01	2.4×10^{-5}	0.02

Note: $L_{HONO} = j_{HONO}$[HONO].

Appendix B: Quantification of isotopic fractionation factor

B1 Nighttime processes

B1.1 Isotopic fractionation of N and O associated with nighttime uptake

Surface uptake is the major sink for HONO during the night. Surface uptake of HONO has been found to be kinetically limited by bulk diffusion in particles containing viscous organic-water matrices, and it incorporates two simultaneous processes: (1) reactive uptake of HONO on the bare particle/mineral surface and (2) accommodation and reaction of HONO in the bulk aqueous layer that is affected by pH and diffusion in the organic-water matrix (Donaldson et al., 2014b). The uptake coefficient of HONO is determined by the competition between these two processes as a function of fraction of water coverage on the surfaces, θ_{H_2O}, ranging from 0 to 1 in Eq. (B1), where γ_0 and γ_1 are the reactive uptake coefficients of HONO onto particle (mineral/soil) surfaces at dry ($\theta_{H_2O} = 0$) and wet ($\theta_{H_2O} = 1$) conditions, respectively. Under completely dry conditions ($\theta_{H_2O} = 0$ or relative humidity (RH) = 0 %), the former process is dominant, and the isotopic fractionation can be estimated by the ratio of the square root of inverse mass, which is caused by different thermal velocities (ω_{HONO}) of two isotopologues following Eq. (B2), where R is the gas constant, T is absolute temperature, and M is the molecular weight. Thus, heavier isotopes are depleted in HONO, resulting in -10 ‰ and -20 ‰ for $^{15}\varepsilon$ and $^{18}\varepsilon$, respectively. By contrast, under wet conditions when RH is 30 % which results in a monolayer water coverage on particle surfaces ($\theta_{H_2O} = 1$), the aqueous layer uptake becomes dominant, and the wet uptake coefficient γ_1 can be mechanistically simulated with a resistor model simplified as Eq. (B3) (Hanson, 1997; Pöschl et al., 2007). In Eq. (B3), α is the accommodation coefficient describing the probability that a HONO molecule striking a water-coated particle enters into the bulk liquid phase, and Γ_b is the solubility of HONO in the bulk water in the particles or soils. Γ_b can be calculated with Eq. (B4), where D_a is the apparent diffusion coefficient of HONO in the particle–water (soil (organics)–water) matrix, and τ is the exposure time. H_{eff} is the effective Henry's law constant that depends on the absolute Henry's law constant for HONO, pH, and acid dissociation constants for HONO (K_{a1}) and $H_2NO_2^+$ (K_{a2}).

$$\gamma_{HONO} = \left(1 - \theta_{H_2O}\right)\gamma_0 + \theta_{H_2O}\,\gamma_1 \quad \text{(B1)}$$

$$\omega_{HONO} = \sqrt{\frac{8RT}{\pi M}} \quad \text{(B2)}$$

$$\gamma_1 = \left(\frac{1}{\alpha} + \frac{1}{\Gamma_b}\right)^{-1} \quad \text{(B3)}$$

$$\Gamma_b = \frac{4H_{eff}RT}{\omega_{HONO}}\sqrt{\frac{D_a}{\pi\tau}} \quad \text{(B4)}$$

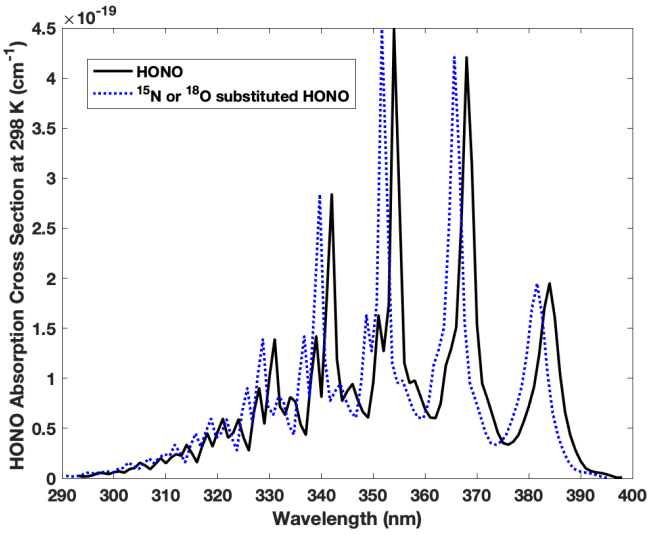

Figure B1. Absorption wavelengths shift for $HO^{15}NO$, $H^{18}ONO$ and $HON^{18}O$ compared with the most abundant form of HONO ($H^{16}O^{14}N^{16}O$). The spectra of $HO^{15}NO$, trans-$H^{18}ONO$ and trans-$HON^{18}O$ are blue shifted 0.23–0.43, 0.21–0.39 and 0.25–0.46 nm, respectively, spanning 293–398 nm. Note that the blue shift illustrated here is 2 nm (larger than the actual shift) in order to demonstrate the shift clearly.

$$k_{u\text{-HONO}} \propto \frac{\gamma_1 \times \omega_{HONO}}{4} \quad \text{(B5)}$$

Taking the previously measured HONO γ_1 of 2×10^{-5} as that for the light isotopologue and α of 5.8×10^{-5} as a constant (Donaldson et al., 2014b), Γ_b ($H^{16}O^{14}N^{16}O$) is calculated to be 1.36×10^{-5} following Eq. (B3). As derived from Eqs. (B2) and (B4), Γ_b ratio between two isotopologues equals the ratio between the two molecular weights, and therefore $\Gamma_b(H^{16}O^{15}N^{16}O)$ and $\Gamma_b(H^{16}O^{15}N^{16}O)$ were calculated and used to derive the corresponding γ_1 values. The fractionation factor associated with HONO uptake ($\alpha_{u\text{-HONO}}$), defined as the ratio between heavy and light rate coefficients (k_H/k_L), was calculated following the relationship determined by Eq. (B5). On the basis of this model, we estimate that the isotopic fractionation associated with the wet uptake process is -2 ‰ and -4 ‰ for $^{15}\varepsilon$ and $^{18}\varepsilon$, respectively. From our calculation, RH clearly influences isotopic fractionation in the range of 0 %–30 %, with the wet uptake of HONO favoring a smaller kinetic isotope effect than dry uptake.

B1.2 Isotopic fractionation of N and O associated with each nighttime HONO production pathway

Heterogeneous conversion of NO_2 to HONO has been widely accepted as the major secondary HONO production source during the night. However, the mechanism via which the conversion occurs remains disputed. Additionally, the kinetic isotopic fractionation factor (KIF) associated with this pro-

Table B1. Vibrational frequencies of HONO and its isotopologues.

Vibrational mode	Vibrational frequency of trans-HONO (cm^{-1})				Vibrational frequency of cis-HONO (cm^{-1})			
	ν (*t*-HONO)	$\Delta\nu$ (*t*-HO^{15}NO)	$\Delta\nu$ (*t*-H^{18}ONO)	$\Delta\nu$ (*t*-HON^{18}O)	ν (*c*-HONO)	$\Delta\nu$ (*c*-HO^{15}NO)	$\Delta\nu$ (*c*-H^{18}ONO)	$\Delta\nu$ (*c*-HON^{18}O)
ν1 (O–H stretch)	3590.71	0.01	12.17	0.01	3426.2	0.01	11.57	0
ν2 (O = N stretch)	1699.76	32.5	0.27	39.28	1640.52	31.54	3.21	31.56
ν3 (HON bending)	1263.21	1.62	10.02	1.39	1302	0.57	8.89	6.24
ν4 (O–N stretch)	790.12	15.73	10.76	2.14	851.94	12.47	21.38	2.57
ν5 (O–N–O bending)	595.6	2.88	14.91	13.96	609	1.95	3.62	1.23
ν6 (torsion)	543	1.25	1.11	1.26	638.5	6.27	7.28	14.91
ΔZPE (cm^{-1})		27	24.62	29.02		26.41	27.98	28.26

cess has never been measured or calculated. NO_2 hydrolysis (Reaction R6) on a variety of surfaces was determined to be a major source of HONO production. A compelling mechanism proposed by Finlayson-Pitts (Finlayson-Pitts et al., 2003) suggests Reaction (R6) consists of a series of key steps including (1) dimer N_2O_4 formation from the recombination of two NO_2 molecules in the gas phase and uptake of gaseous N_2O_4 by thin water film on the top surface layer, (2) aqueous-phase isomerization of symmetric N_2O_4 to asymmetric $ONONO_2$ which is subsequently autoionizing to $NO^+NO_3^-$ and reacting with H_2O to form HONO and HNO_3, and (3) desorption of HONO from aqueous to gas phase. Recently it was shown that reduction of NO_2 on iron-bearing minerals and quinone-rich humic acid in soils and particulate matter (Reaction R7) leads to faster HONO production than NO_2 hydrolysis. Although differing in reaction mechanism, the two possible pathways (Reactions R6 and R7) proceed in three steps including uptake of NO_2 into the surface aqueous layer, reactions in aqueous phase and desorption of HONO from aqueous to gas phase. The first two steps are limited by aqueous diffusion, and it is reasonable to assume diffusion-limited processes in the aqueous phase create no KIF. As HONO desorption may involve hydrogen bond breaking of complex HONO–$(H_2O)_n$, this process likely determines the KIF associated with the heterogeneous NO_2-to-HONO conversion (α_d), as calculated by Eq. (B6), where μ_l and μ_h are the reduced mass for the light and heavy isotope containing pair, respectively (Shi et al., 2019). As a result, $^{15}\varepsilon$ and $^{18}\varepsilon$ are estimated to be -2.9 ‰ ($n = 1$) to -4.5 ‰ ($n = 2$) and -5.7 ‰ ($n = 1$) to -8.9 ‰ ($n = 2$), respectively. For the isotope mass balance modeling, mean values of $^{15}\varepsilon$ (3.7 ‰) and $^{18}\varepsilon$ (7.4 ‰) were generally used for steady-state Reactions (R3), (R6) and (R7) under steady-state conditions, and the low ($n = 2$) and high ($n = 1$) values were used to evaluate the lower and upper bound.

$$\alpha_d = \sqrt{\mu_l/\mu_h} \tag{B6}$$

B2 Daytime

B2.1 HONO photolysis

The isotopic effect associated with photolysis (PIE) of HONO is calculated for the first time following the ΔZPE approach proposed by Yung and Miller (1997) to determine the PIE of N_2O photolysis. In principle, the absorption spectrum for the same kind of electronic transition is expected to be similar in shape and intensity upon isotopic substitution, based on the assumption that the electronic potential energy surface is constant for each isotopologue. This assures the continuum levels (leading to photolysis) of the excited state are not significantly changed, while the vibrational levels of the ground state vary with isotopic substitutions due to mass difference. The latter results in a lower ground state zero point energy (ZPE) for a heavy isotopologue than a light one and causes blue shift in the absorption spectrum of the heavy isotopologue relative to the light one (Miller and Yung, 2000). When exposed to sunlight in the troposphere (>290 nm), HONO is known to feature a set of progressive absorption bands between 310 and 370 nm arising from electronic excitation ($\widetilde{X}^1A' \rightarrow \widetilde{A}^1A''$), which results in HONO photolysis to OH and NO with nearly unity quantum yield (Cox et al., 1980; Suter and Huber, 1989). Under the aforementioned assumptions, we calculate the spectra blue shift of all three heavy isotopologues (HO^{15}NO, H^{18}ONO or HON^{18}O) relative to that of HONO using the ΔZPE approach as shown in Fig. B1 and Tables B1 and B2.

We calculated ΔZPE from $1/2\Sigma\Delta\nu_i$, where $\Delta\nu_i$ is the ground state vibrational frequency difference between the normal isotopologue (HONO) and the heavier isotopologue (HO^{15}NO, H^{18}ONO or HON^{18}O) for each vibrational mode calculated via forced field by Monse et al. (1969). Note only HO^{15}NO UV absorption was measured in a previous study that reported an average blue shift of $\sim$20 cm^{-1} (8–40 cm^{-1}) relative to HONO, and this is consistent with our calculation (Table B1). Note trans-HONO / cis-HONO abundance ratio is 2.5 at room temperature (Suter and Huber, 1989), and the difference of ΔZPE for trans-HONO and cis-HONO is less than 0.5 % for ^{15}N and 2 % for ^{18}O (Ta-

Table B2. Parameters used for TUV solar actinic flux modeling. The modeled enrichment coefficients for HONO photolysis for $HO^{15}NO$, $H^{18}ONO$ and $HON^{18}O$ are presented in a data repository (https://doi.org/10.26300/k056-fs32).

Start time (MDT)	Latitude	Longitude	Altitude (m)	j(HONO) s^{-1}	$j(HO^{15}NO)$ s^{-1}	$j(H^{18}ONO)$ s^{-1}	$j(HON^{18}O)$ s^{-1}	ε^{15} ‰	ε ($H^{18}ONO$) ‰	ε ($HON^{18}O$) ‰
08/16/18 15:56	44.6726	−114.2339	1700	1.412E-03	1.408E-03	1.408E-03	1.407E-03	−2.6	−2.2	−3.0
08/16/18 17:51	44.6726	−114.2339	1700	9.319E-04	9.287E-04	9.291E-04	9.283E-04	−3.4	−3.0	−3.8
08/09/18 15:38	44.5048	−114.2320	1500	1.486E-03	1.482E-03	1.483E-03	1.482E-03	−2.5	−2.2	−2.9
08/09/18 19:10	45.3870	−113.9619	1117	4.733E-04	4.724E-04	4.726E-04	4.722E-04	−1.9	−1.4	−2.3
08/14/18 10:38	44.7173	−114.0226	1412	1.257E-03	1.253E-03	1.254E-03	1.253E-03	−2.8	−2.4	−3.3
08/14/18 17:18	44.7173	−114.0226	1412	1.101E-03	1.098E-03	1.098E-03	1.097E-03	−3.1	−2.7	−3.5
08/14/18 12:00	44.7173	−114.0226	1412	1.496E-03	1.492E-03	1.492E-03	1.491E-03	−2.5	−2.2	−2.9
08/14/18 13:30	44.7173	−114.0226	1412	1.596E-03	1.592E-03	1.593E-03	1.592E-03	−2.4	−2.1	−2.8
08/14/18 15:00	44.7173	−114.0226	1412	1.534E-03	1.530E-03	1.531E-03	1.530E-03	−2.5	−2.1	−2.8
08/14/18 17:22	44.7173	−114.0226	1412	1.085E-03	1.082E-03	1.082E-03	1.081E-03	−3.2	−2.7	−3.4
08/14/18 20:11	44.7173	−114.0226	1412	1.027E-04	1.023E-04	1.024E-04	1.023E-04	−4.2	−3.7	−4.7
08/14/18 18:40	44.7173	−114.0226	1412	6.329E-04	6.304E-04	6.307E-04	6.302E-04	−3.9	−3.5	−4.3
08/10/18 09:50	45.3870	−113.9619	1117	1.052E-03	1.049E-03	1.046E-03	1.045E-03	−3.2	−5.5	−6.3
08/10/18 20:26	45.3870	−113.9619	1117	7.373E-05	7.342E-05	7.346E-05	7.339E-05	−4.3	−3.7	−4.7
08/10/18 12:00	45.3870	−113.9619	1117	1.495E-03	1.491E-03	1.491E-03	1.490E-03	−2.6	−2.2	−2.9
08/10/18 14:00	45.3870	−113.9619	1117	1.592E-03	1.588E-03	1.589E-03	1.587E-03	−2.4	−2.0	−2.8
08/10/18 16:00	45.3870	−113.9619	1117	1.403E-03	1.400E-03	1.400E-03	1.399E-03	−2.7	−2.3	−3.0
08/10/18 18:00	45.3870	−113.9619	1117	9.014E-04	8.984E-04	8.988E-04	8.980E-04	−3.4	−2.9	−3.8

ble B1). The effect of the difference on j calculation is negligible. With the measured absorption cross-section of HONO between 293 and 400 nm and the quantified blue shift of all three isotopologues, we calculate each photolysis rate coefficient following Eq. (B7), which is the integral of photolysis quantum yield $\Phi_a(\lambda)$ ($\approx$1), absorption cross-section $\sigma_a(\lambda)$ and solar actinic flux $I(\lambda)$ as a function of wavelength. $I(\lambda)$ is computed with the radiation transfer model TUV (http://www.acd.ucar.edu/TUV, Madronich and Flocke, 1998) at various locations and times during our sampling period. With these j values listed in Table B2 (j, $j_{^{15}N}$, $j_{^{18}O_1}$, $j_{^{18}O_2}$), the fractionation constant ($^{15}\varepsilon$ and $^{18}\varepsilon$, ‰) associated with HONO photolysis is calculated following Eq. (B8), where j' and j are photolysis rate coefficients of heavy and light isotopologues, respectively. Note we take the average of $j_{^{18}O_1}$ and $j_{^{18}O_2}$ as $j_{^{18}O}$ assuming the ^{18}O is equally distributed between the two O sites of HONO. Results show that $^{15}\varepsilon$ and $^{18}\varepsilon$ range from −1.9 ‰ to −4.3 ‰ (mean = −3.0 ‰, 1σ = 0.7 ‰, n = 18 ‰) and −1.9 ‰ to −5.9 ‰ (mean = −3.1 ‰, 1σ = 1.0 ‰, n = 18 ‰), respectively, when the HONO photolysis rate decreases from 1.4×10^{-3} to 5.3×10^{-4} s^{-1}.

$$j = \int \sigma_a(\lambda)\, \Phi_a(\lambda)\, I(\lambda)\, d(\lambda) \tag{B7}$$

$$\varepsilon = \left[\left(\frac{j'}{j}\right) - 1\right] \times 1000\,‰ \tag{B8}$$

The negative values of $^{15}\varepsilon$ and $^{18}\varepsilon$ suggest both ^{15}N and ^{18}O will be enriched in the remaining HONO upon photolysis. Applying a Rayleigh fractionation model described by equation Eq. (B9), we obtain $\delta^{15}N$ and $\delta^{18}O$ of HONO (δ_f) as a function of the fraction of HONO left after photolysis (f). The initial isotopic composition of HONO (δ_0) is taken from nighttime young smoke mean values in Table 1, as they are the best estimate of the fresh emission from the fires we investigated.

$$\ln\left(\delta_f + 1000\,‰\right) = \varepsilon \ln(f) + \ln(\delta_0 + 1000‰) \tag{B9}$$

B2.2 Isotopic fractionation of N and O associated with each daytime HONO production pathway

OH + NO (Reaction R2) is a radical–radical recombination reaction, which is characteristic of the stabilization of activated complex HONO* via collisional energy transfer. This reaction type is characteristic of large KIF that enriches heavier isotopologues in the product at the low-pressure limit but almost no KIF at the high-pressure limit. The closer a reaction system is to the high-pressure limit, the less fractionation occurs (Chai and Dibble, 2014). Under the atmospheric pressure, the rate coefficient k_1 is in the fall-off region but close to the high-pressure limiting rate coefficient $k_{atm} = 1/3k^{\infty}$ (Forster et al., 1995). Therefore, we expect a moderate positive $^{15}\varepsilon$ ($\sim$ 10 ‰) and $^{18}\varepsilon$ ($\sim$ 15 ‰) (Chai and Dibble, 2014; Burkholder et al., 2019). Kinetic isotopic fractionation (KIF) associated with photo-enhanced NO_2 conversion is not known. Similar to the nighttime heterogeneous NO_2 conversion, Reaction (R3) is also expected to occur in the surface aqueous phase, and the overall KIF is largely determined by that associated with the desorption of HONO from aqueous to gas phase. Thus, $^{15}\varepsilon_3$ and $^{18}\varepsilon_3$ are the same as that of Reactions (R6) and (R7) (Appendix B1.2).

KIF associated with HNO_3 and p-NO_3^- photolysis (Reaction R4) in the atmosphere has never been measured experimentally, and the lack of p-NO_3^- absorption spectroscopy hinders calculation. The ^{15}N enrichment factor ($^{15}\varepsilon$) for photolysis of snow-surface-adsorbed HNO_3 under natural sun-

light was theoretically determined to be $\leq -47.9\,‰$ following the ΔZPE approach Yung and Miller (1997), which explained well the laboratory-measured $^{15}\varepsilon$ for snow surface nitrate photolysis under the radiation of simulated sunlight (Berhanu et al., 2014; Frey et al., 2009). If we take this $^{15}\varepsilon$ value and the measured δ^{15}N of nitrate (8 ‰ to 20 ‰), the HONO produced from surface nitrate photolysis will be very negative (−38.9 ‰ to −27.5 ‰) within 2 h of photolysis. The ^{18}O enrichment factor ($^{18}\varepsilon$) for photolysis of snow-surface-adsorbed HNO_3 has been measured to range from 6.0 ‰ to 12.5 ‰ (Frey et al., 2009; Berhanu et al., 2015).

B3 The δ^{18}O transferring coefficient by different pathways

For ^{18}O, in addition to KIF (enrichment factor, $\varepsilon^i_{\mathrm{O}}$ in ‰), δ^{18}O transferring from different reactants greatly influence δ^{18}O-HONO ($\delta^{18}O_{i,t}$), especially when the two O atoms of HONO are derived from different reactants. That is, HONO formed from different pathways (Reactions R2, R3, R6, R7) consists of δ^{18}O of each O-containing reacting partner in a proportion determined by stoichiometry of reaction i, expressed with Eqs. (10)–(12). In Reaction (R2), OH and NO equally contribute their O atom to HONO expressed with Eq. (10). In Reactions (R3) and (R7), NO_2 is the exclusive O source of HONO, while H_3O^+ only contributes a H^+ to HONO (Ammann et al., 1998; George et al., 2005; Stemmler et al., 2006; Scharko et al., 2017; Kebede et al., 2016). In Reaction (R6), the hydrolysis mechanism discussed in Appendix B suggests the H_2O-derived OH^- and NO_2-derived $NO^+NO_3^-$ equally contribute their O atom to HONO (Finlayson-Pitts et al., 2003).

$$\delta^{18}O_{2,t} = \frac{1}{2}\delta^{18}O{-}OH + \frac{1}{2}\delta^{18}O{-}NO \tag{B10}$$

$$\delta^{18}O_{3(\text{or } 7),t} = \delta^{18}O{-}NO_2 \tag{B11}$$

$$\delta^{18}O_{6,t} = \frac{1}{2}\delta^{18}O - H_2O + \frac{1}{2}\delta^{18}O - NO_2 \tag{B12}$$

During the day, NO–NO_2 equilibrium is maintained via NO_2 photolysis and NO oxidation by O_3 and/or RO_2 following Reactions (R8) and (R9), and NO and NO_2 are expected to possess similar δ^{18}O, and this can be expressed as δ^{18}O-NO_x. During the night, due to increased sink of NO_x and decreased O_3 concentration, δ^{18}O-NO_x is expected to be lower than during daytime. NO_x resulting from Reactions (R8) and (R9) should carry δ^{18}O of RO_2 and O_3, respectively, via transfer; as RO_2 and O_3 have very different δ^{18}O values $\sim +23\,‰$ and $+117\,‰$, respectively, the competition between Reactions (R8) and (R9) critically affects δ^{18}O-NO_x, as described by equations Eqs. (11) and (12). OH radical in the troposphere has been calculated to be $-35\,‰$ depleted in ^{18}O relative to H_2O as a result of isotopic exchange at 298 K (Walters and Michalski, 2016); by taking the ^{18}O values for summertime precipitation water in the western US (−10 ‰ to −5 ‰) (Welker, 2000) and the H_2O liquid-to-vapor enrichment factor ε_{g-l} of +9 ‰ at 298 K derived from the literature with Eq. (B13) (Michalski et al., 2012), δ^{18}O-OH is estimated in the range of −35 ‰ to −30 ‰ if we ignore the unknown KIF derived from OH oxidation reaction with the vast majority of atmospheric species. The overall δ^{18}O-HONO is modeled using the isotope mass balance model.

$$\varepsilon_{g-l} = -7.68 + 6.71\left(\frac{10^3}{T}\right) - 1.67\left(\frac{10^6}{T^2}\right) + 0.35\left(\frac{10^9}{T^3}\right) \tag{B13}$$

Data availability. All data are available in the manuscript, the Supplement or data repository (https://doi.org/10.26300/k056-fs32) (Chai, 2020).

Supplement. The supplement related to this article is available online at: https://doi.org/10.5194/acp-21-13077-2021-supplement.

Author contributions. JED and MH conceived the research. JC, JED and MGH designed the research. JC carried out field sampling, laboratory sample analyses, data analyses and figure production, as well as conceived and carried out the isotopic box modeling work. BEA, CEJ, WWW, DEB, EEJ, JHK, HM and EH contributed to field sampling. CB helped with laboratory sample analyses. JC wrote the paper. All authors contributed to the scientific discussions and preparation of the manuscript.

Competing interests. The authors declare that they have no conflict of interest.

Disclaimer. Any mention of brand names or manufacturers is for information purposes only and does not constitute an endorsement.

Publisher's note: Copernicus Publications remains neutral with regard to jurisdictional claims in published maps and institutional affiliations.

Acknowledgement. We thank the entire FIREX-AQ team and WE-CAN team, especially Robert Yokelson and the Aerodyne Research Mobile Lab team. We also thank the United States Forest Service for the field support. We are grateful to Ruby Ho for laboratory support. We are particularly thankful that Thomas Ryerson and Jeff Peischl generously let us use the NOAA mobile lab and for their support during the WE-CAN field season. We acknowledge James Roberts and two other anonymous reviewers for their helpful comments.

Financial support. This research has been supported by the National Science Foundation (grant no. 1351932) and the National Oceanic and Atmospheric Administration (grant no. NA16OAR4310098).

Review statement. This paper was edited by Christopher Cantrell and reviewed by James Roberts and two anonymous referees.

References

Akagi, S. K., Yokelson, R. J., Wiedinmyer, C., Alvarado, M. J., Reid, J. S., Karl, T., Crounse, J. D., and Wennberg, P. O.: Emission factors for open and domestic biomass burning for use in atmospheric models, Atmos. Chem. Phys., 11, 4039–4072, https://doi.org/10.5194/acp-11-4039-2011, 2011.

Akagi, S. K., Craven, J. S., Taylor, J. W., McMeeking, G. R., Yokelson, R. J., Burling, I. R., Urbanski, S. P., Wold, C. E., Seinfeld, J. H., Coe, H., Alvarado, M. J., and Weise, D. R.: Evolution of trace gases and particles emitted by a chaparral fire in California, Atmos. Chem. Phys., 12, 1397–1421, https://doi.org/10.5194/acp-12-1397-2012, 2012.

Alvarado, M. J. and Prinn, R. G.: Formation of ozone and growth of aerosols in young smoke plumes from biomass burning: 1. Lagrangian parcel studies, J. Geophys. Res.-Atmos., 114, D09306, https://doi.org/10.1029/2008JD011144, 2009.

Alvarado, M. J., Logan, J. A., Mao, J., Apel, E., Riemer, D., Blake, D., Cohen, R. C., Min, K.-E., Perring, A. E., Browne, E. C., Wooldridge, P. J., Diskin, G. S., Sachse, G. W., Fuelberg, H., Sessions, W. R., Harrigan, D. L., Huey, G., Liao, J., Case-Hanks, A., Jimenez, J. L., Cubison, M. J., Vay, S. A., Weinheimer, A. J., Knapp, D. J., Montzka, D. D., Flocke, F. M., Pollack, I. B., Wennberg, P. O., Kurten, A., Crounse, J., Clair, J. M. S., Wisthaler, A., Mikoviny, T., Yantosca, R. M., Carouge, C. C., and Le Sager, P.: Nitrogen oxides and PAN in plumes from boreal fires during ARCTAS-B and their impact on ozone: an integrated analysis of aircraft and satellite observations, Atmos. Chem. Phys., 10, 9739–9760, https://doi.org/10.5194/acp-10-9739-2010, 2010.

Alvarado, M. J., Lonsdale, C. R., Yokelson, R. J., Akagi, S. K., Coe, H., Craven, J. S., Fischer, E. V., McMeeking, G. R., Seinfeld, J. H., Soni, T., Taylor, J. W., Weise, D. R., and Wold, C. E.: Investigating the links between ozone and organic aerosol chemistry in a biomass burning plume from a prescribed fire in California chaparral, Atmos. Chem. Phys., 15, 6667–6688, https://doi.org/10.5194/acp-15-6667-2015, 2015.

Ammann, M., Kalberer, M., Jost, D. T., Tobler, L., Rössler, E., Piguet, D., Gäggeler, H. W., and Baltensperger, U.: Heterogeneous production of nitrous acid on soot in polluted air masses, Nature, 395, 157–160, https://doi.org/10.1038/25965, 1998.

Baergen, A. M. and Donaldson, D. J.: Photochemical Renoxification of Nitric Acid on Real Urban Grime, Environ. Sci. Technol., 47, 815–820, https://doi.org/10.1021/es3037862, 2013.

Baergen, A. M. and Donaldson, D. J.: Formation of reactive nitrogen oxides from urban grime photochemistry, Atmos. Chem. Phys., 16, 6355–6363, https://doi.org/10.5194/acp-16-6355-2016, 2016.

Baylon, P., Jaffe, D. A., Hall, S. R., Ullmann, K., Alvarado, M. J., and Lefer, B. L.: Impact of Biomass Burning Plumes on Photolysis Rates and Ozone Formation at the Mount Bachelor Observatory, J. Geophys. Res.-Atmos., 123, 2272–2284, https://doi.org/10.1002/2017JD027341, 2018.

Berhanu, T. A., Meusinger, C., Erbland, J., Jost, R., Bhattacharya, S. K., Johnson, M. S., and Savarino, J.: Laboratory study of nitrate photolysis in Antarctic snow, II. Isotopic effects and wavelength dependence, J. Chem. Phys., 140, 244306, https://doi.org/10.1063/1.4882899, 2014.

Berhanu, T. A., Savarino, J., Erbland, J., Vicars, W. C., Preunkert, S., Martins, J. F., and Johnson, M. S.: Isotopic effects of nitrate photochemistry in snow: a field study at Dome C, Antarctica, Atmos. Chem. Phys., 15, 11243–11256, https://doi.org/10.5194/acp-15-11243-2015, 2015.

Böhlke, J. K., Mroczkowski, S. J., and Coplen, T. B.: Oxygen isotopes in nitrate: new reference materials for 18O:17O:16O measurements and observations on nitrate-water equilibra-

tion, Rapid Commun. Mass Spectrom., 17, 1835–1846, https://doi.org/10.1002/rcm.1123, 2003.

Burkholder, J. B., Sander, S. P., Abbatt, J., Barker, J. R., Cappa, C., Crounse, J. D., Dibble, T. S., Huie, R. E., Kolb, C. E., Kurylo, M. J., Orkin, V. L., Percival, C. J., Wilmouth, D. M. and Wine P. H.: Chemical Kinetics and Photochemical Data for Use in Atmospheric Studies, Evaluation No. 19, JPL Publication 19-5, Jet Propulsion Laboratory, Pasadena, 2019.

Casciotti, K. L., Sigman, D. M., Hastings, M. G., Böhlke, J. K., and Hilkert, A.: Measurement of the Oxygen Isotopic Composition of Nitrate in Seawater and Freshwater Using the Denitrifier Method, Anal. Chem., 74, 4905–4912, https://doi.org/10.1021/ac020113w, 2002.

Chai, J.: Isotopic evidence for dominant secondary production of HONO in near-ground wildfire plumes, Brown University Open Data Collection, Brown Digital Repository [data set], Brown University Library, https://doi.org/10.26300/k056-fs32 (last access: 15 January 2021), 2020.

Chai, J. and Dibble, T. S.: Pressure Dependence and Kinetic Isotope Effects in the Absolute Rate Constant for Methoxy Radical Reacting with NO_2, Int. J. Chem. Kinet., 46, 501–511, https://doi.org/10.1002/kin.20865, 2014.

Chai, J. and Hastings, M.: Collection Method for Isotopic Analysis of Gaseous Nitrous Acid, Anal. Chem., 90, 830–838, https://doi.org/10.1021/acs.analchem.7b03561, 2018.

Chai, J., Miller, D. J., Scheuer, E., Dibb, J., Selimovic, V., Yokelson, R., Zarzana, K. J., Brown, S. S., Koss, A. R., Warneke, C., and Hastings, M.: Isotopic characterization of nitrogen oxides (NO_x), nitrous acid (HONO), and nitrate (pNO_3^-) from laboratory biomass burning during FIREX, Atmos. Meas. Tech.,12, 6303–6317, https://doi.org/10.5194/amt-12-6303-2019, 2019.

Cox, R. A., Derwent, R. G., Kearsey, S. V., Batt, L., and Patrick, K. G.: Photolysis of methyl nitrite: kinetics of the reaction of the methoxy radical with O_2, J. Photochem., 13, 149–163, https://doi.org/10.1016/0047-2670(80)85006-4, 1980.

de Gouw, J. A., Warneke, C., Stohl, A., Wollny, A. G., Brock, C. A., Cooper, O. R., Holloway, J. S., Trainer, M., Fehsenfeld, F. C., Atlas, E. L., Donnelly, S. G., Stroud, V., and Lueb, A.: Volatile organic compounds composition of merged and aged forest fire plumes from Alaska and western Canada, J. Geophys. Res.-Atmos., 111, D10303, https://doi.org/10.1029/2005JD006175, 2006.

Donaldson, M. A., Bish, D. L., and Raff, J. D.: Soil surface acidity plays a determining role in the atmospheric-terrestrial exchange of nitrous acid, P. Natl. Acad. Sci. USA, 111, 18472–18477, https://doi.org/10.1073/pnas.1418545112, 2014a.

Donaldson, M. A., Berke, A. E., and Raff, J. D.: Uptake of Gas Phase Nitrous Acid onto Boundary Layer Soil Surfaces, Environ. Sci. Technol., 48, 375–383, https://doi.org/10.1021/es404156a, 2014b.

Fibiger, D. L. and Hastings, M. G.: First Measurements of the Nitrogen Isotopic Composition of NO_x from Biomass Burning, Environ. Sci. Technol., 50, 11569–11574, https://doi.org/10.1021/acs.est.6b03510, 2016.

Fibiger, D. L., Hastings, M. G., Lew, A. F., and Peltier, R. E.: Collection of NO and NO_2 for Isotopic Analysis of NO_x Emissions, Anal. Chem., 86, 12115–12121, https://doi.org/10.1021/ac502968e, 2014.

Finlayson-Pitts, B. J., Wingen, L. M., Sumner, A. L., Syomin, D., and Ramazan, K. A.: The heterogeneous hydrolysis of NO_2 in laboratory systems and in outdoor and indoor atmospheres: An integrated mechanism, Phys. Chem. Chem. Phys., 5, 223–242, https://doi.org/10.1039/B208564J, 2003.

Fischer, E. V., Jaffe, D. A., Reidmiller, D. R., and Jaeglé, L.: Meteorological controls on observed peroxyacetyl nitrate at Mount Bachelor during the spring of 2008, J. Geophys. Res.-Atmos., 115, https://doi.org/10.1029/2009JD012776, 2010.

Forster, R., Frost, M., Fulle, D., Hamann, H. F., Hippler, H., Schlepegrell, A., and Troe, J.: High pressure range of the addition of HO to HO, NO, NO_2, and CO, I. Saturated laser induced fluorescence measurements at 298 K, J. Chem. Phys., 103, 2949–2958, https://doi.org/10.1063/1.470482, 1995.

Frey, M. M., Savarino, J., Morin, S., Erbland, J., and Martins, J. M. F.: Photolysis imprint in the nitrate stable isotope signal in snow and atmosphere of East Antarctica and implications for reactive nitrogen cycling, Atmos. Chem. Phys., 9, 8681–8696, https://doi.org/10.5194/acp-9-8681-2009, 2009.

George, C., Strekowski, R. S., Kleffmann, J., Stemmler, K., and Ammann, M.: Photoenhanced uptake of gaseous NO_2 on solid organic compounds: a photochemical source of HONO?, Faraday Discuss., 130, 195–210, https://doi.org/10.1039/b417888m, 2005.

Hanson, D. R.: Surface-Specific Reactions on Liquids, J. Phys. Chem. B, 101, 4998–5001, https://doi.org/10.1021/jp970461f, 1997.

Hastings, M. G., Jarvis, J. C., and Steig, E. J.: Anthropogenic Impacts on Nitrogen Isotopes of Ice-Core Nitrate, Science, 324, 1288–1288, https://doi.org/10.1126/science.1170510, 2009.

Jaffe, D. and Briggs, N.: Ozone production from wildfires: A critical review, Atmos. Environ., 51, 1–10, https://doi.org/10.1016/j.atmosenv.2011.11.063, 2012.

Jaffe, D. A., Wigder, N., Downey, N., Pfister, G., Boynard, A., and Reid, S. B.: Impact of Wildfires on Ozone Exceptional Events in the Western U.S., Environ. Sci. Technol., 47, 11065–11072, https://doi.org/10.1021/es402164f, 2013.

Kaspari, J. H., Chai, J., Anderson, B. E., Jordan, C. E., Scheuer, E., Hastings, M. G., Dibb, J. E.: Influence of Solar Irradiation on Nitrous Acid Production in Western U.S. Wildfire Smoke, Earth Space Sci. Open Arch., https:/doi.org/10.1002/essoar.10506007.1, last access: 15 February 2021.

Kebede, M. A., Bish, D. L., Losovyj, Y., Engelhard, M. H., and Raff, J. D.: The Role of Iron-Bearing Minerals in NO_2 to HONO Conversion on Soil Surfaces, Environ. Sci. Technol., 50, 8649–8660, https://doi.org/10.1021/acs.est.6b01915, 2016.

Kleinman, L. I., Daum, P. H., Lee, Y.-N., Senum, G. I., Springston, S. R., Wang, J., Berkowitz, C., Hubbe, J., Zaveri, R. A., Brechtel, F. J., Jayne, J., Onasch, T. B., and Worsnop, D.: Aircraft observations of aerosol composition and ageing in New England and Mid-Atlantic States during the summer 2002 New England Air Quality Study field campaign, J. Geophys. Res.-Atmos., 112, D09310, https://doi.org/10.1029/2006JD007786, 2007.

Liu, X., Zhang, Y., Huey, L. G., Yokelson, R. J., Wang, Y., Jimenez, J. L., Campuzano-Jost, P., Beyersdorf, A. J., Blake, D. R., Choi, Y., Clair, J. M. S., Crounse, J. D., Day, D. A., Diskin, G. S., Fried, A., Hall, S. R., Hanisco, T. F., King, L. E., Meinardi, S., Mikoviny, T., Palm, B. B., Peischl, J., Perring, A. E., Pollack, I.

B., Ryerson, T. B., Sachse, G., Schwarz, J. P., Simpson, I. J., Tanner, D. J., Thornhill, K. L., Ullmann, K., Weber, R. J., Wennberg, P. O., Wisthaler, A., Wolfe, G. M., and Ziemba, L. D.: Agricultural fires in the southeastern U.S. during SEAC4RS: Emissions of trace gases and particles and evolution of ozone, reactive nitrogen, and organic aerosol, J. Geophys. Res.-Atmos., 121, 7383–7414, https://doi.org/10.1002/2016JD025040, 2016.

Madronich, S., Flocke, F. M., Zeng, J., Petropavlovskikh, I., and Lee-Taylor, J.: Tropospheric Ultraviolet and Visible (TUV) Radiation Model, available at: https://www.acom.ucar.edu/Models/TUV/Interactive_TUV/ (last access: 17 March 2020), 2002.

Mark, C. A.: Salmon-Challis National Forest: Salmon-Challis national forest assessment report, available at: https://www.fs.usda.gov/detail/scnf/landmanagement/planning/?cid=fseprd544724 (last access: 12 December 2020), 2018.

Martins-Costa, M. T. C., Anglada, J. M., Francisco, J. S., and Ruiz-López, M. F.: The Aqueous Surface as an Efficient Transient Stop for the Reactivity of Gaseous NO_2 in Liquid Water, J. Am. Chem. Soc., 142, 20937–20941, https://doi.org/10.1021/jacs.0c10364, 2020.

McClure, C. D. and Jaffe, D. A.: US particulate matter air quality improves except in wildfire-prone areas, P. Natl. Acad. Sci. USA, 115, 7901–7906, https://doi.org/10.1073/pnas.1804353115, 2018.

Michalski, G., Scott, Z., Kabiling, M., and Thiemens, M. H.: First measurements and modeling of $\Delta^{17}O$ in atmospheric nitrate, Geophys. Res. Lett., 30, 1870, https://doi.org/10.1029/2003GL017015, 2003.

Michalski, G., Bhattacharya, S. K., and Mase, D. F.: Oxygen Isotope Dynamics of Atmospheric Nitrate and Its Precursor Molecules, in: Handbook of Environmental Isotope Geochemistry, Springer, Berlin, Heidelberg, 30, 613–635, https://doi.org/10.1007/978-3-642-10637-8_30, 2012.

Miller, C. E. and Yung, Y. L.: Photo-induced isotopic fractionation, J. Geophys. Res.-Atmos., 105, 29039–29051, https://doi.org/10.1029/2000JD900388, 2000.

Miller, D. J., Wojtal, P. K., Clark, S. C., and Hastings, M. G.: Vehicle NO_x emission plume isotopic signatures: Spatial variability across the eastern United States, J. Geophys. Res.-Atmos., 122, 4698–4717, https://doi.org/10.1002/2016JD025877, 2017.

Monse, E. U., Spindel, W., and Stern, M. J.: Analysis of Isotope-effect Calculations Illustrated with Exchange Equilibria Among Oxynitrogen Compounds, in: Isotope Effects in Chemical Processes, Am. Chem. Soc., 89, 148–184, https://doi.org/10.1021/ba-1969-0089.ch009, 1969.

Ndour, M., D'Anna, B., George, C., Ka, O., Balkanski, Y., Kleffmann, J., Stemmler, K., and Ammann, M.: Photoenhanced uptake of NO_2 on mineral dust: Laboratory experiments and model simulations, Geophys. Res. Lett., 35, L05812, https://doi.org/10.1029/2007GL032006, 2008.

Nie, W., Ding, A. J., Xie, Y. N., Xu, Z., Mao, H., Kerminen, V.-M., Zheng, L. F., Qi, X. M., Huang, X., Yang, X.-Q., Sun, J. N., Herrmann, E., Petäjä, T., Kulmala, M., and Fu, C. B.: Influence of biomass burning plumes on HONO chemistry in eastern China, Atmos. Chem. Phys., 15, 1147–1159, https://doi.org/10.5194/acp-15-1147-2015, 2015.

Parrington, M., Palmer, P. I., Lewis, A. C., Lee, J. D., Rickard, A. R., Di Carlo, P., Taylor, J. W., Hopkins, J. R., Punjabi, S., Oram, D. E., Forster, G., Aruffo, E., Moller, S. J., Bauguitte, S. J.-B., Allan, J. D., Coe, H., and Leigh, R. J.: Ozone photochemistry in boreal biomass burning plumes, Atmos. Chem. Phys., 13, 7321–7341, https://doi.org/10.5194/acp-13-7321-2013, 2013.

Peng, Q., Palm, B. B., Melander, K. E., Lee, B. H., Hall, S. R., Ullmann, K., Campos, T., Weinheimer, A. J., Apel, E. C., Hornbrook, R. S., Hills, A. J., Montzka, D. D., Flocke, F., Hu, L., Permar, W., Wielgasz, C., Lindaas, J., Pollack, I. B., Fischer, E. V., Bertram, T. H., and Thornton, J. A.: HONO Emissions from Western U.S. Wildfires Provide Dominant Radical Source in Fresh Wildfire Smoke, Environ. Sci. Technol., 54, 5954–5963, https://doi.org/10.1021/acs.est.0c00126, 2020.

Platt, U., Perner, D., Harris, G. W., Winer, A. M., and Pitts, J. N.: Observations of nitrous acid in an urban atmosphere by differential optical absorption, Nature, 285, 312–314, https://doi.org/10.1038/285312a0, 1980.

Pöschl, U., Rudich, Y., and Ammann, M.: Kinetic model framework for aerosol and cloud surface chemistry and gas-particle interactions – Part 1: General equations, parameters, and terminology, Atmos. Chem. Phys., 7, 5989–6023, https://doi.org/10.5194/acp-7-5989-2007, 2007.

Scharko, N. K., Martin, E. T., Losovyj, Y., Peters, D. G., and Raff, J. D.: Evidence for Quinone Redox Chemistry Mediating Daytime and Nighttime NO_2-to-HONO Conversion on Soil Surfaces, Environ. Sci. Technol., 51, 9633–9643, https://doi.org/10.1021/acs.est.7b01363, 2017.

Scheuer, E., Talbot, R. W., Dibb, J. E., Seid, G. K., DeBell, L., and Lefer, B.: Seasonal distributions of fine aerosol sulfate in the North American Arctic basin during TOPSE, J. Geophys. Res.-Atmos., 108, 8370, https://doi.org/10.1029/2001JD001364, 2003.

Selimovic, V., Yokelson, R. J., McMeeking, G. R., and Coefield, S.: In situ measurements of trace gases, PM, and aerosol optical properties during the 2017 NW US wildfire smoke event, Atmos. Chem. Phys., 19, 3905–3926, https://doi.org/10.5194/acp-19-3905-2019, 2019.

Selimovic, V., Yokelson, R. J., McMeeking, G. R., and Coefield, S.: Aerosol Mass and Optical Properties, Smoke Influence on O_3, and High NO_3 Production Rates in a Western U.S. City Impacted by Wildfires, J. Geophys. Res.-Atmos., 125, e2020JD032791, https://doi.org/10.1029/2020JD032791, 2020.

Shi, G., Chai, J., Zhu, Z., Hu, Z., Chen, Z., Yu, J., Ma, T., Ma, H., An, C., Jiang, S., Tang, X., and Hastings, M. G.: Isotope Fractionation of Nitrate During Volatilization in Snow: A Field Investigation in Antarctica, Geophys. Res. Lett., 46, 3287–3297, https://doi.org/10.1029/2019GL081968, 2019.

Sigman, D. M., Casciotti, K. L., Andreani, M., Barford, C., Galanter, M., and Böhlke, J. K.: A Bacterial Method for the Nitrogen Isotopic Analysis of Nitrate in Seawater and Freshwater, Anal. Chem., 73, 4145–4153, https://doi.org/10.1021/ac010088e, 2001.

Spataro, F. and Ianniello, A.: Sources of atmospheric nitrous acid: State of the science, current research needs, and future prospects, J. Air Waste Manage., 64, 1232–1250, https://doi.org/10.1080/10962247.2014.952846, 2014.

Stemmler, K., Ammann, M., Donders, C., Kleffmann, J., and George, C.: Photosensitized reduction of nitrogen dioxide on humic acid as a source of nitrous acid, Nature, 440, 195–198, https://doi.org/10.1038/nature04603, 2006.

Stockwell, C. E., Yokelson, R. J., Kreidenweis, S. M., Robinson, A. L., DeMott, P. J., Sullivan, R. C., Reardon, J., Ryan, K. C., Griffith, D. W. T., and Stevens, L.: Trace gas emissions from combustion of peat, crop residue, domestic biofuels, grasses, and other fuels: configuration and Fourier transform infrared (FTIR) component of the fourth Fire Lab at Missoula Experiment (FLAME-4), Atmos. Chem. Phys., 14, 9727–9754, https://doi.org/10.5194/acp-14-9727-2014, 2014.

Su, H., Cheng, Y., Oswald, R., Behrendt, T., Trebs, I., Meixner, F. X., Andreae, M. O., Cheng, P., Zhang, Y., and Pöschl, U.: Soil Nitrite as a Source of Atmospheric HONO and OH Radicals, Science, 333, 1616–1618, https://doi.org/10.1126/science.1207687, 2011.

Suter, H. U. and Huber, J. R.: S_1 potential energy surface of HONO: Absorption spectrum and photodissociation, Chem. Phys. Lett., 155, 203–209, https://doi.org/10.1016/0009-2614(89)85350-3, 1989.

Talukdar, R. K., Burkholder, J. B., Schmoltner, A.-M., Roberts, J. M., Wilson, R. R., and Ravishankara, A. R.: Investigation of the loss processes for peroxyacetyl nitrate in the atmosphere: UV photolysis and reaction with OH, J. Geophys. Res.-Atmos., 100, 14163–14173, https://doi.org/10.1029/95JD00545, 1995.

Theys, N., Volkamer, R., Müller, J.-F., Zarzana, K. J., Kille, N., Clarisse, L., De Smedt, I., Lerot, C., Finkenzeller, H., Hendrick, F., Koenig, T. K., Lee, C. F., Knote, C., Yu, H., and Van Roozendael, M.: Global nitrous acid emissions and levels of regional oxidants enhanced by wildfires, Nat. Geosci., 13, 681–686, https://doi.org/10.1038/s41561-020-0637-7, 2020.

Thiemens, M. H.: History and Applications of Mass-Independent Isotope Effects, Annu. Rev. Earth Planet. Sci., 34, 217–262, https://doi.org/10.1146/annurev.earth.34.031405.125026, 2006.

Tuite, K., Thomas, J. L., Veres, P. R., Roberts, J. M., Stevens, P. S., Griffith, S. M., Dusanter, S., Flynn, J. H., Ahmed, S., Emmons, L., Kim, S.-W., Washenfelder, R., Young, C., Tsai, C., Pikelnaya, O., and Stutz, J.: Quantifying nitrous acid formation mechanisms using measured vertical profiles during the CalNex 2010 campaign and 1D column modeling, J. Geophys. Res.-Atmos, 126, e2021JD034689, https://doi.org/10.1029/2021JD034689, 2021.

VandenBoer, T. C., Young, C. J., Talukdar, R. K., Markovic, M. Z., Brown, S. S., Roberts, J. M., and Murphy, J. G.: Nocturnal loss and daytime source of nitrous acid through reactive uptake and displacement, Nat. Geosci., 8, 55–60, https://doi.org/10.1038/ngeo2298, 2014.

Walters, W. W. and Michalski, G.: Theoretical calculation of nitrogen isotope equilibrium exchange fractionation factors for various NO_y molecules, Geochim. Cosmochim. Ac., 164, 284–297, https://doi.org/10.1016/j.gca.2015.05.029, 2015.

Walters, W. W. and Michalski, G.: Theoretical calculation of oxygen equilibrium isotope fractionation factors involving various NO_y molecules, OH, and H_2O and its implications for isotope variations in atmospheric nitrate, Geochim. Cosmochim. Ac., 191, 89–101, https://doi.org/10.1016/j.gca.2016.06.039, 2016.

Walters, W. W., Fang, H., and Michalski, G.: Summertime diurnal variations in the isotopic composition of atmospheric nitrogen dioxide at a small midwestern United States city, Atmos. Environ., 179, 1–11, https://doi.org/10.1016/j.atmosenv.2018.01.047, 2018.

Welker, J. M.: Isotopic ($\delta^{18}O$) characteristics of weekly precipitation collected across the USA: an initial analysis with application to water source studies, Hydrol. Process., 14, 1449–1464, https://doi.org/10.1002/1099-1085(20000615)14:8<1449::AID-HYP993>3.0.CO;2-7, 2000.

Westerling, A. L.: Increasing western US forest wildfire activity: sensitivity to changes in the timing of spring, Phil. Trans. R. Soc. B, 371, 20150178, https://doi.org/10.1098/rstb.2015.0178, 2016.

Westerling, A. L., Hidalgo, H. G., Cayan, D. R., and Swetnam, T. W.: Warming and Earlier Spring Increase Western U.S. Forest Wildfire Activity, Science, 313, 940–943, https://doi.org/10.1126/science.1128834, 2006.

Wojtal, P. K., Miller, D. J., O'Conner, M., Clark, S. C., and Hastings, M. G.: Automated, High-resolution Mobile Collection System for the Nitrogen Isotopic Analysis of NO_x, J. Vis. Exp., 118, e54962, https://doi.org/10.3791/54962, 2016.

Wong, K. W., Tsai, C., Lefer, B., Haman, C., Grossberg, N., Brune, W. H., Ren, X., Luke, W., and Stutz, J.: Daytime HONO vertical gradients during SHARP 2009 in Houston, TX, Atmos. Chem. Phys., 12, 635–652, https://doi.org/10.5194/acp-12-635-2012, 2012.

Wong, K. W., Tsai, C., Lefer, B., Grossberg, N., and Stutz, J.: Modeling of daytime HONO vertical gradients during SHARP 2009, Atmos. Chem. Phys., 13, 3587–3601, https://doi.org/10.5194/acp-13-3587-2013, 2013.

Ye, C., Zhou, X., Pu, D., Stutz, J., Festa, J., Spolaor, M., Tsai, C., Cantrell, C., Mauldin, R. L., Campos, T., Weinheimer, A., Hornbrook, R. S., Apel, E. C., Guenther, A., Kaser, L., Yuan, B., Karl, T., Haggerty, J., Hall, S., Ullmann, K., Smith, J. N., Ortega, J., and Knote, C.: Rapid cycling of reactive nitrogen in the marine boundary layer, Nature, 532, 489–491, https://doi.org/10.1038/nature17195, 2016.

Ye, C., Zhang, N., Gao, H., and Zhou, X.: Photolysis of Particulate Nitrate as a Source of HONO and NO_x, Environ. Sci. Technol., 51, 6849–6856, https://doi.org/10.1021/acs.est.7b00387, 2017.

Yokelson, R. J., Crounse, J. D., DeCarlo, P. F., Karl, T., Urbanski, S., Atlas, E., Campos, T., Shinozuka, Y., Kapustin, V., Clarke, A. D., Weinheimer, A., Knapp, D. J., Montzka, D. D., Holloway, J., Weibring, P., Flocke, F., Zheng, W., Toohey, D., Wennberg, P. O., Wiedinmyer, C., Mauldin, L., Fried, A., Richter, D., Walega, J., Jimenez, J. L., Adachi, K., Buseck, P. R., Hall, S. R., and Shetter, R.: Emissions from biomass burning in the Yucatan, Atmos. Chem. Phys., 9, 5785–5812, https://doi.org/10.5194/acp-9-5785-2009, 2009.

Yung, Y. L. and Miller, C. E.: Isotopic Fractionation of Stratospheric Nitrous Oxide, 278, 1778–1780, https://doi.org/10.1126/science.278.5344.1778, 1997.

Zhou, X., Zhang, N., TerAvest, M., Tang, D., Hou, J., Bertman, S., Alaghmand, M., Shepson, P. B., Carroll, M. A., Griffith, S., Dusanter, S., and Stevens, P. S.: Nitric acid photolysis on forest canopy surface as a source for tropospheric nitrous acid, Nat. Geosci., 4, 440–443, https://doi.org/10.1038/ngeo1164, 2011.